Nuclear Instruments and Methods in Physics Research A313 (1992) 63–102
North-Holland

NUCLEAR INSTRUMENTS & METHODS IN PHYSICS RESEARCH
Section A

The Mark II silicon strip vertex detector *

C. Adolphsen, R.G. Jacobsen and V. Lüth
Stanford Linear Accelerator Center, Stanford University, Stanford, CA 94309, USA

G. Gratta [1], L. Labarga [2], A.M. Litke, A.S. Schwarz [3], M. Turala [4] and C. Zaccardelli [5]
Santa Cruz Institute for Particle Physics, University of California, Santa Cruz, CA 95064, USA

A. Breakstone, C.J. Kenney and S.I. Parker
University of Hawaii, Honolulu, HI 96822, USA

B.A. Barnett, P. Dauncey [6], D.C. Drewer and J.A.J. Matthews [7]
Johns Hopkins University, Baltimore, MD 21218, USA

Received 3 September 1991

A silicon strip vertex detector consisting of 36 modules has been built and operated in the Mark II solenoidal detector at the Stanford Linear Collider. The construction of the detector modules, their performance tests, the stability and accuracy of their placement, and the precision alignment of the complete device prior to and after installation are discussed. We also describe the operation of the vertex detector, and we discuss the measurement of impact parameters of charged particle tracks in conjunction with the Mark II wire drift chambers.

1. Design concepts for the vertex detector

1.1. Introduction

In recent years, experiments at the e^+e^- storage rings PEP, PETRA, DORIS, and CESR have demonstrated that vertex detectors with moderate resolution (50–120 μm) can substantially enhance the detection efficiency and signal-to-noise ratio for the decays of heavy leptons and heavy flavor hadrons. To date, the only measurements of the lifetime of the $\tau^{\pm}$ lepton and the average lifetime of B hadrons have been performed with drift chambers operating at these storage rings. Following the successful employment of silicon microstrip detectors as vertex detectors in fixed target experiments [1], and the development of custom VLSI readout electronics [2,3], we proposed in 1985 to build a silicon strip vertex detector for the Mark II experiment [4] at the Stanford Linear Collider. The goal was to provide a few high precision point measurements as close to the beam–beam interaction point as practical and thereby complement the angle and momentum measurements in the central drift chamber (CDC) [5]. With an expected position resolution of about 5 μm per point, the addition of a silicon vertex detector was expected to improve, for high momentum charged particles, the resolution in the impact parameter relative to the beam–beam interaction point by more than a factor of 10. In addition, the fine granularity of the

* Work supported by the US Department of Energy, contracts DE-AC03-76SF00515, DE-AC-83ER040103, and DE-AA03-76SF00034 and by the US National Science Foundation Grant 87 01 610.

[1] Fellow of the Istituto Nazionale di Fisica Nucleare, Rome, Italy; present address: CERN, EP Division, Genève, Switzerland.
[2] Present address: Universidad Autónoma, Madrid, Spain.
[3] Present address: Max-Planck Institut für Physik und Astrophysik, München, Germany.
[4] Visitor from the Institute of Nuclear Physics, Krakow, Poland.
[5] Present address: CERN, EP-Division, Genève, Switzerland.
[6] Present address: Oxford University, Oxford, UK.
[7] Present address: University of New Mexico, Albuquerque, NM 87131, USA.

silicon strip detectors would provide the ability to resolve tracks that are separated by as little as 5 mrad and to thereby reduce errors in track recognition.

The primary motivation for the construction of a high resolution vertex detector at the Stanford Linear Collider (SLC) was its potential to tag the presence of heavy flavor hadrons in the decay of the Z^0 resonance. The ability to identify decays of particles with lifetimes in the range 10^{-12} to 10^{-13}, both inclusively and exclusively, permits access to a wide range of fundamental physics questions, such as the test of the coupling of the charged and neutral weak current to charm and beauty quarks via the measurement of the lifetimes of charm and beauty hadrons or via measurements of the branching ratios of the Z^0 to $\bar{c}c$ and $\bar{b}b$. Furthermore, the sensitivity to new particles such as the Higgs that are expected to decay to heavy leptons or quarks is substantially increased by the detection of secondary vertices.

The potential for vertex detection was greatly enhanced by three unique features that a single pass collider, such as the SLC, could offer:

- a beam–beam interaction volume of less than 10 μm in diameter and 1.5 mm in length that could allow for a precise location of the primary vertex;
- a vacuum pipe of 5 cm or less in diameter that permitted the placement of a detector within a radial distance of 3 cm from the beam line; this substantially enhanced the impact parameter resolution and also reduced the total area of the detector needed to cover a given solid angle; and
- a beam crossing frequency of 120 Hz that allowed for a small duty cycle and therefore low average power consumption of the readout electronics.

In this article, the design, construction, and installation of the three layer silicon strip detector for the Mark II experiment will be described. This will include a discussion of the design goals and constraints, the performance tests of the detector modules, measurements of radiation hardness as well as methods for precision alignment of the completed device prior to and after installation. We also present results on the operation of the vertex detector inside the Mark II solenoidal detector, in particular the measurement of the impact parameters of charged particle tracks in conjunction with external wire drift chambers.

1.2. Design constraints and goals

The silicon strip vertex detector (SSVD) was proposed for the Mark II experiment at the same time as and constructed in parallel to the jet-cell vertex drift chamber (VDC) [6,7]. Both devices were designed to complement each other and to provide the best possible measurement of the impact parameters of charged tracks. The precision drift chamber was to provide 32

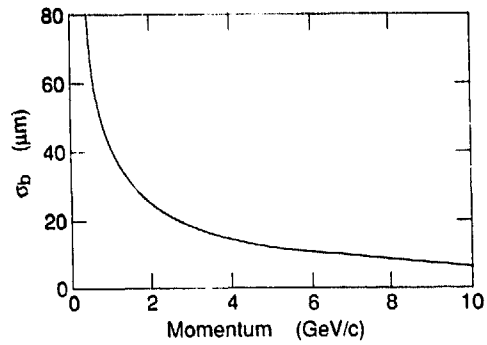

Fig. 1. Calculated impact parameter resolution, σ_b, as a function of the momentum of tracks produced at 90° to the beam axis.

measurements per track and a long lever arm for pattern recognition resulting in a precise measurement of the azimuthal angle. The silicon vertex detector was to measure a few points with very high precision close to the beam and to resolve two tracks down to a separation of 5 mrad. Fig. 1 shows the expected impact parameter resolution as a function of the charged particle track momentum. The curve is a calculation taking into account the expected position resolution of the three tracking devices (170 μm for the CDC, 40 μm for the VDC, and 5 μm for a 3-layer silicon strip detector) and the contribution from multiple scattering in the vacuum pipe and the detectors. The calculation assumed perfect track reconstruction and a priori knowledge of the beam–beam interaction point. Uncertainties in the detector alignment and beam motion, and errors in pattern recognition due to the high density of hits from tracks and beam background were expected to degrade the resolution. However, they would not have a severe impact on the physics potential of the vertex detector system.

In the following, the specific design goals for the SSVD as well as the constraints imposed by the surrounding VDC and other components of the Mark II detector [4] are discussed.

1) Since tracks from the decays of heavy flavor particles have typical impact parameters between 100 and 300 μm, a high efficiency for the detection of their decays and a high purity of the selected sample required a resolution in the impact parameter on the order of 20 μm for particle momenta of a few GeV/c.

2) The SSVD had to fit into an annulus defined by the inner wall of the VDC at 44 mm and the outer radius of the central, thin-walled section of the vacuum pipe at 26 mm. The inner radius of the vacuum pipe was defined by the radial extent of the synchrotron radiation background generated in the final focus quadrupoles. This severe space limitation ruled out the use of conventional electronics. The amplifier and readout electronics had to be fabricated in VLSI tech-

nology and were custom-designed. Multiplexed readout as well as miniaturized signal fan-outs and cables were necessary to fit the cable plant into the extremely limited space.

3) The solid angle coverage had to correspond to that of the VDC and the CDC, about 80% of 4π. In practice, the solid angle coverage was determined by the maximum detector length that could be cut from the largest high purity silicon wafer available, i.e., 10 cm in diameter.

4) The amount of material in the active region of the detector was to be minimized to reduce multiple scattering, conversions of photons, and interactions of particles originating both from Z^0 decays as well as from beam generated background.

5) In the presence of dense jets and sizable beam background, multiple layers and a high detection efficiency per layer were required to provide redundancy and thereby suppress tracking errors. With measurements in two or more layers, track angles could be determined to allow for the matching with track elements in the vertex and central drift chambers. Given that it would be difficult to avoid gaps between detectors in a given layer, and the fact that there was not sufficient radial space to overlap detector edges within a layer, this meant that the number of layers had to be three. The third layer would also provide constraints necessary for the relative alignment of the individual detectors based on particle tracks.

6) Though it was desirable to improve the rather limited resolution of the CDC in the z coordinate parallel to the beam, the silicon detector was designed to measure only the azimuthal angle ϕ at a given radius. For a first generation silicon detector at a colliding beam machine it was thought to be prudent not to attempt two-dimensional detector design and readout.

7) To assure the correct matching of track elements in jet-like events produced in Z^0 decays, the SSVD had to have the ability to separate tracks that were separated by as little as 5 mrad in azimuth. At the inner radius of the SSVD, this meant that two-track separation down to 150 μm was needed, a performance that had already been achieved in a beam test [8].

8) The excellent intrinsic resolution of the detectors placed stringent demands on the alignment and rigidity of the support structure. The detector modules had to be placed with an accuracy of 50 μm and had to be stable to a few μm over many weeks of operation. The exact location of the individual detector modules had to be determined to an accuracy that was considerably better than the detector resolution.

9) The detector and the associated electronics had to be able to withstand the radiation produced by the SLC beams. Even though the annual dosage for normal operation was estimated to be very low, roughly 20 rad, background calculations were known to be unreliable, in particular for a machine of completely novel design. Also, background rates generated during the commissioning of a new accelerator were likely to exceed those during normal operation. It was therefore prudent to aim at a system that would be resistant to radiation levels that were higher than the estimates by 2–3 orders of magnitude.

In summary, the construction of the silicon strip vertex detector for the Mark II detector required the design and fabrication of a) single sided detectors with strip lengths of up to 9 cm and a position resolution of 10 μm or better, b) custom-designed integrated amplifier and readout circuits with a radiation hardness of 20 krad, c) miniaturized signal fanouts and cables, d) a stable support structure and e) the development of precision techniques for the alignment of a multilayer detector in three dimensions.

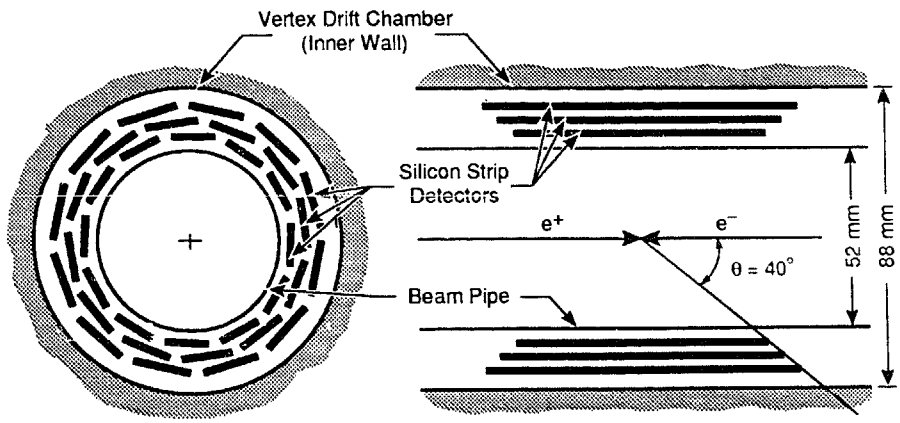

Fig. 2. Schematic layout of the silicon strip vertex detector with the vacuum pipe on the inside and the vertex drift chamber on the outside.

1.3. Detector layout

A brief description of the SSVD is given here as an introduction to the more detailed description of the design and fabrication that follows. The basic layout of the SSVD is shown schematically in fig. 2. There were 3 layers with 12 detectors each, and 512 strips per detector, resulting in a total of 18432 strips. The strips were parallel to the axis of the beam, thus the detectors measured positions in the plane transverse to the beam, the $x-y$ or $r-\phi$ plane. The detector relied on the central drift chamber to provide momentum and z measurements. The length and width of the detectors increased from layer to layer so as to maintain a simple geometry and to achieve an azimuthal coverage of 85% of 2π for each of the three layers. This was realized by choosing strip pitches of 25, 29, and 33 μm for the three layers. In each layer, a single detector spanned a polar angle range comparable to the large central tracking chamber, namely $|\cos\phi| < 0.77$. This simplified the implementation of the design and was made possible by the fabrication of detectors on 10 cm diameter silicon wafers [9].

The detectors were read out from both ends by two pairs of custom-designed VLSI chips with 128 channels each, the so-called "Microplex" [2,3]. Alternate strips at each end were wirebonded to the Microplex chips that received power and timing signals from adjacent hybrid circuits. A single thin cable connected the two ends and the hybrids with the external microprocessor-controlled data acquisition system. The hybrid circuits and the Microplex chips were placed outside the active area of the detectors and therefore did not contribute to the multiple scattering.

The individual detectors were assembled in modules that were designed to operate as independent units with their own power supply and readout. The modules were inserted into two half-cylindrical support structures that were mounted on the central section of the vacuum pipe at the SLC interaction point. To monitor the position of the SSVD relative to the surrounding vertex drift chamber, capacitive probes were placed on the outside enclosure of the SSVD, outside the active area of the detector.

2. The silicon strip detector

2.1. Detector design and dimensions

Ion implanted silicon strip detectors for use in high energy physics were first developed by Kemmer [10] and are now commercially available. These detectors are made from high purity monocrystal silicon. They consist of a large number of reversed bias microstrip diode junctions formed in a substrate of n-type silicon with dopant concentrations of about $10^{12}/cm^3$. The bulk material is sandwiched between a thin layer of highly doped n-type silicon on the bottom and strips of p^+ implants with aluminium contacts on the top. A positive voltage is applied to a metal electrode covering the n^+ implant on the bottom. The top surface of the detectors is resin-coated for protection. Electron–hole pairs created by ionizing radiation are separated by the electric field and the charges moving towards the conducting electrodes then generate an electrical signal.

Table 1
Properties of the silicon strip detectors

Detector property	Layer I	Layer II	Layer III	Units
Layer radius	29.4	33.7	38.0	mm
Strip pitch	25	29	33	μm
Strip width	8	8	8	μm
Number of strips	512	512	512	
Detector size	13.8×74.8	15.8×85.1	17.9×93.5	mm^2
Sensitive area	12.9×72.0	14.9×82.0	17.0×90.0	mm^2
Thickness	314	314	314	μm
Capacitance to other strips	8.2	8.8	9.3	pF
Capacitance to back plane	0.6	0.8	1.0	pF

The detector dimensions and properties for the three layers are listed in table 1. The detectors were custom-designed, prototyped, and manufactured for this experiment by Hamamatsu Photonics KK of Japan and represented the first silicon strip detectors fabricated from 10 cm diameter wafers. Details of the layout of the readout section are shown in fig. 3. At each detector end, alternate strips were connected (dc coupled) to pads for wirebonding to the readout electronics. Each pad was 150 μm long and 100 μm wide. The bonding pads had a pitch of 200 μm and were arranged in four rows. For detectors with a strip pitch

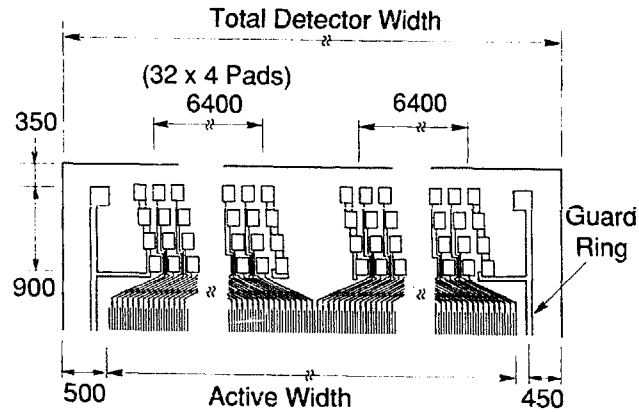

Fig. 3. Details of the readout portion of a silicon detector showing the bonding pads, signal fan-ins and guard ring. All dimensions are given in μm.

of more than 25 μm, the signal lines were fanned in so as to have a common bonding pad configuration for all detectors.

A p^+ implant surrounding the active area of the detector served as a guard ring and protected the active strips against leakage currents from the detector edges. The guard ring was set back from the physical edge of the detector by 450 μm. In this design, the guard ring passed below the conducting traces which connected the strips to the bonding pads and then to the inputs of the front-end electronics. As a result, a fast signal on the guard ring could capacitively couple directly to all front-end amplifiers. An example of this effect is shown in fig. 4. The pedestal pattern was caused by the variation in the geometric overlap between the guard ring and the signal lines crossing on the surface (see fig. 3). The problem was cured by connecting a high frequency capacitive filter to the guard ring.

All detectors were expected to fully deplete at a bias voltage of 75 V or less. Limits on the initial leakage currents per strip were guaranteed by the manufacturer. For all but a few strips per detector, the leakage current was specified to be less than 20 nA at 10 V above the full depletion voltage, and no more than two strips were to exceed 200 nA.

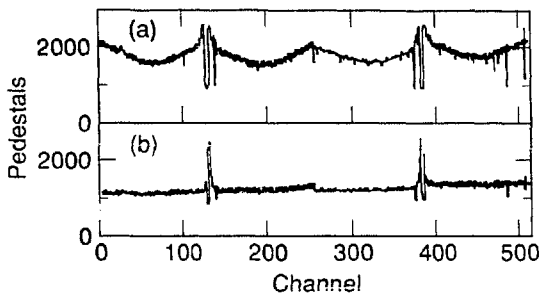

Fig. 4. Histogram of pedestals (in units of the ADC) versus strip number, for a detector (a) without and (b) with a capacitive bypass to ground. The pattern is generated by the variation of the capacitance between the guard ring and the signal fan-ins to the bonding pads.

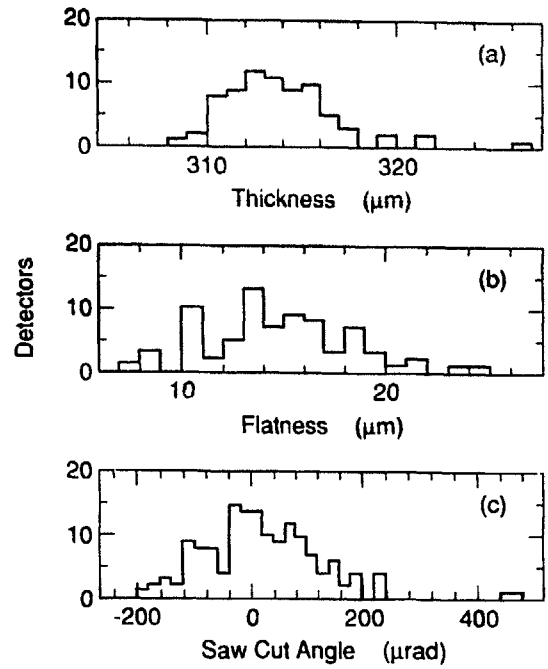

Fig. 5. Mechanical properties of the detectors: (a) the thickness, (b) the flatness, measured as the maximum deviation from a fitted plane and (c) the angle of the saw cut edges relative to the strips.

2.2. Mechanical properties

A number of measurements were performed to check the mechanical tolerances of the detectors that were delivered by the manufacturer. In particular, the detector thickness, flatness, and the alignment of the saw cut edges relative to the detector strips were checked. All of these measurements were performed using a measuring microscope with a precision of about 4 μm. The results are shown in fig. 5.

2.2.1. Detector thickness

The detector thickness was measured at six points along the periphery. Within the measuring accuracy, all detectors were found to have uniform thickness over surface. However, for different detectors, the thickness varied between 309 and 327 μm; the average thickness of all detectors was 314 μm.

2.2.2. Detector flatness

The flatness of the detectors was measured while they were supported at the ends on a set of gauge blocks. The coordinates for points on the detector surface were recorded. The data were fit to a plane and the maximum deviation from the fitted plane was used as a measure of the flatness. All detectors were found to be slightly bowed, with a deviation from flatness of 14.3 μm on average. Roughly half of this bow could be explained as gravitational sag. The concern here was that an aplanarity would translate into a measurement error for tracks that have non-normal incidence. However, the observed effects were small and the observed shape allowed for a simple geometric correction. More importantly, the shape of the installed detector was actually determined by the placement of the module in the support structure rather than by the initial detector shape.

2.2.3. Saw cuts

The individual detectors were cut from the silicon wafer with a diamond saw that was aligned to cut parallel to the strips on the detector. The accuracy of the placement of the cut was specified to be ±0.25

mrad. Since we were planning to use the detector edges as reference during the assembly of the modules, we measured the alignment of the saw cuts with respect to the detector strips. For this measurement, one of the detector edges was placed against two reference pins on a jig. The orientation of the first detector strip was measured relative to the detector edge defined by the pins. The measurement was performed separately for both detector edges, and in general the results were found to be highly correlated, i.e. the two saw cuts were parallel to each other. On average, the uncertainty of the individual measurements was of the order of 0.05 mrad, largely due to the roughness of the saw cut. The average angle of the detector strips relative to the detector edges was 0.044 mrad.

2.3. Depletion voltage

To assure full charge collection, the operation of a silicon detector requires that the silicon be fully depleted. The depth of the depletion layer, W, increases with the reverse bias voltage, $W \propto \sqrt{V_{det}}$. This relation holds until the detector is fully depleted, i.e. W equals the thickness of the detector. Since the depletion depth is inversely proportional to the capacitance across the diode junction, it can be determined by measuring this capacitance as a function of the bias voltage. Fig. 6 shows an example of a depletion voltage measurement and the circuit diagram that was used. The data were fit to a pair of straight lines, one of constant capacitance signifying full depletion, and the other with a slope, described by the function $\ln C_{det} = A + B \ln V_{det}$. The value of V_{det} at the intersection was by definition

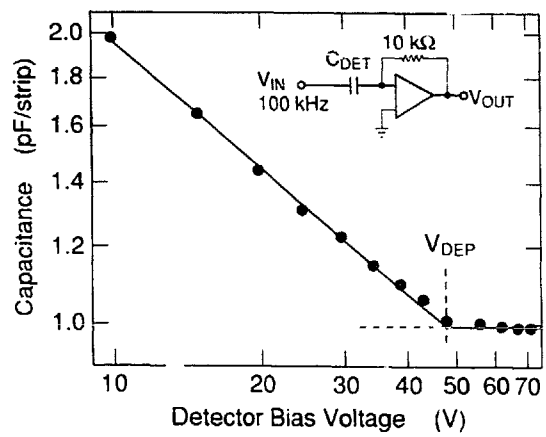

Fig. 6. Depletion voltage measurement for a 90 mm long detector: the strip-to-backplane capacitance is measured as a function of the bias voltage. The lines are explained in the text. The inserted circuit diagram illustrates the use of an operational amplifier for this measurement: a 100 kHz ac voltage is applied to the strips (V_{IN}) and the amplitude of the output voltage is recorded as a function of the detector bias voltage.

the depletion voltage. The procedure was calibrated with capacitances of known size. The values for the slope B ranged from -0.35 to -0.80, in fair agreement with the theoretical expectation of -0.5. The measured capacitances had to be corrected for the substantial contribution from the probe card pins. In some cases, the leakage current across the detector caused a significant drop in the bias voltage and this had to be taken into account. The uncertainty in the measurement of the depletion voltage was estimated to be 2–3 V, and the measurements were not very sensitive to temperature. All of the 76 detectors delivered by Hamamatsu KK depleted between 40 and 70 V, most of them around 45 V. There were significant variations for different batches of detectors produced: for instance, all 8 detectors with a measured depletion voltage above 55 V were part of the same batch.

2.4. Leakage current and interstrip resistance

The operation of the individual strip diodes was checked by a measurement of the leakage current and the resistance between neighboring strips. For the leakage current measurements, 64 detector strips at a time were individually grounded through two 250 kΩ resistors in series, and the current was derived from the drop in voltage across one of the resistors as measured by a scanning DVM. Measurements were performed with the guard ring connected to ground for two different settings of the bias voltage, namely the depletion voltage and 10 V above this voltage. Eight setups were necessary to cover the 512 strips per detector. The tests were performed in complete darkness so as to avoid the response of the diodes to light. The results, obtained at bias voltages 10 V above depletion, were quite remarkable: of the total of 76 detectors (38912 strips) only 12 (4) strips on 6 (4) different detectors showed a leakage current exceeding 200 nA, and 44 (10) strips on 8 (6) detectors exceeded 20 nA. The numbers in the parentheses refer to the results with two detectors with large leakage currents removed from the sample. Most of the strips had leakage currents on the order of 1 nA or less. One of the detectors had a small number of strips shorted to the guard ring.

For a number of detectors, large negative currents were measured when the guard ring was set to -3 V. The size of the current depended on the distance of the strip from the guard ring, i.e., the current was largest for the strip next to the guard ring and decreased with increasing strip number. This effect was found to be caused by low resistance between the diode strips.

To measure the interstrip resistance, a voltage of 50 mV was applied to individual pairs of strips and the current between the strips was measured with a picoamperemeter. The applied voltage was higher than the expected voltage acquired by a strip from the charge

collected from a minimum ionizing particle (0.1 mV) and well below the voltage at which punchthrough effects were expected (2 V). For this sensitive measurement the detector was unbiased and complete darkness was necessary to obtain meaningful results. Because of space constraints for the microprobes there was one floating strip between the strips of a pair. On some detectors, the strip-to-strip resistance was found to be as low as 10–100 Ω compared to a normal value of 1–3 MΩ. The effect was traced to the packaging of the individual detectors during shipping. A rigid plastic support that was in contact with the detector inside a carbon-filled plastic wrapper induced electrostatic charge on the protective coating of the detector. The charges accumulated above the SiO_2 between the p-implants of adjacent strips and induced a conducting channel of holes in the n-type silicon. The effect usually diminished with time after the packaging was removed, but it would take many days until the charge was neutralized and the normal resistance was attained.

The electrostatic charge effect was reduced by a change in the packaging material and by exposure to UV light or ionized air. It was observed that the effect was related to a property of the specific coating applied by the manufacturer. Detectors furnished by a different supplier [11] did not show any evidence of electrostatic build-up, even after exposure to highly charged materials. These detectors had a much higher interstrip resistance, 30 MΩ instead of 3 MΩ.

Because of the potential problems caused by small interstrip resistance, nine or more measurements were performed on each of the 76 detectors more than ten days after they had been removed from the packaging. A total of 21, 9, and 3 detectors showed strips with resistances between 100–1000 kΩ, 10–100 kΩ, and below 10 kΩ, respectively. Since normal operation of the detectors required at least 100 kΩ, the detectors that did not reach this limit were not used for the assembly of modules.

Silicon detectors had been exposed in the past to high intensity beams of charged particles and were known to operate up to doses of several Mrad [12]. To test the radiation resistance, one of the prototype detectors was exposed to a ^{60}Co source delivering an hourly dose of roughly 500 rad. A linear rise in leakage current per strip (surface area of ≈ 1.9 mm^2) was observed, at a rate of roughly 0.1 μA/Mrad at a temperature of about 20°C. For comparison, a current of 400 nA or more would saturate the amplifier.

3. The microplex circuit

The processing of the signals produced by the silicon detectors began with the Microplex chip [2,3]. This custom-designed VLSI circuit was the first of a series that has been developed over the past decade to solve the problem of reading out channels of the high density associated with the use of silicon strip detectors in colliding beam experiments. The chip contained 128 channels of double-correlated sample-and-hold circuitry, together with a multiplexed readout capability, in an area of 6.3 mm (width) × 5.4 mm (length). It was realized using 5 μm NMOS design rules. Prototypes of the chips were designed and fabricated at the Stanford Integrated Circuits Laboratory; the chips used in the production of the SSVD were manufactured commercially [13].

3.1. Basic layout and operation

Fig. 7 shows a block diagram of a single channel of the Microplex chip together with the schematics of its main components. The operation of the circuit proceeded in two stages which were independently controllable. In the first or "analog" stage, the input charge was collected by an integrating amplifier. Its output was connected to two storage capacitors (C_{S1} and C_{S2}) through FET switches. The switch to C_{S1} was opened before, and the switch to C_{S2} was opened after the expected arrival time of a signal. Two pulses, S_1 and S_2, controlled this timing sequence as shown in fig. 8. The voltage difference between C_{S2} and C_{S1} was proportional to the charge integrated during the period between the falling edges of S_1 and S_2. This double-correlated sampling had the advantage of subtracting switching transients occurring before S_1 and any common charge leakage from the two storage capacitors after S_2. Also, the Fourier components of noise with periods much longer than $S_2 - S_1$ were suppressed.

In the second or "digital" stage of the circuit operation, the signals were read out serially. The voltages on the pairs of storage capacitors sequentially controlled the currents in two bus lines (Out_1 and Out_2). The bus connections were made through two FET switches which were closed when a logic pulse (Read Bit) was clocked, channel-to-channel, through a shift register. This clocking sequence is illustrated in fig. 9. The output buses were connected through wire bonds to a differential amplifier on the hybrid circuit to which the chips were attached. These lines were also tied to a high impedance voltage source on the hybrid which effectively made the Microplex output circuit a source follower. The differential amplifier signal was sent via line drivers on the hybrid to a digitizer. The end result of the analog and digital processing was a single number for each channel which was proportional to the current integrated during the S_2–S_1 time interval.

3.2. Details of the design and operation

The connections between the detector and Microplex chips were made by aluminum wire bonds of

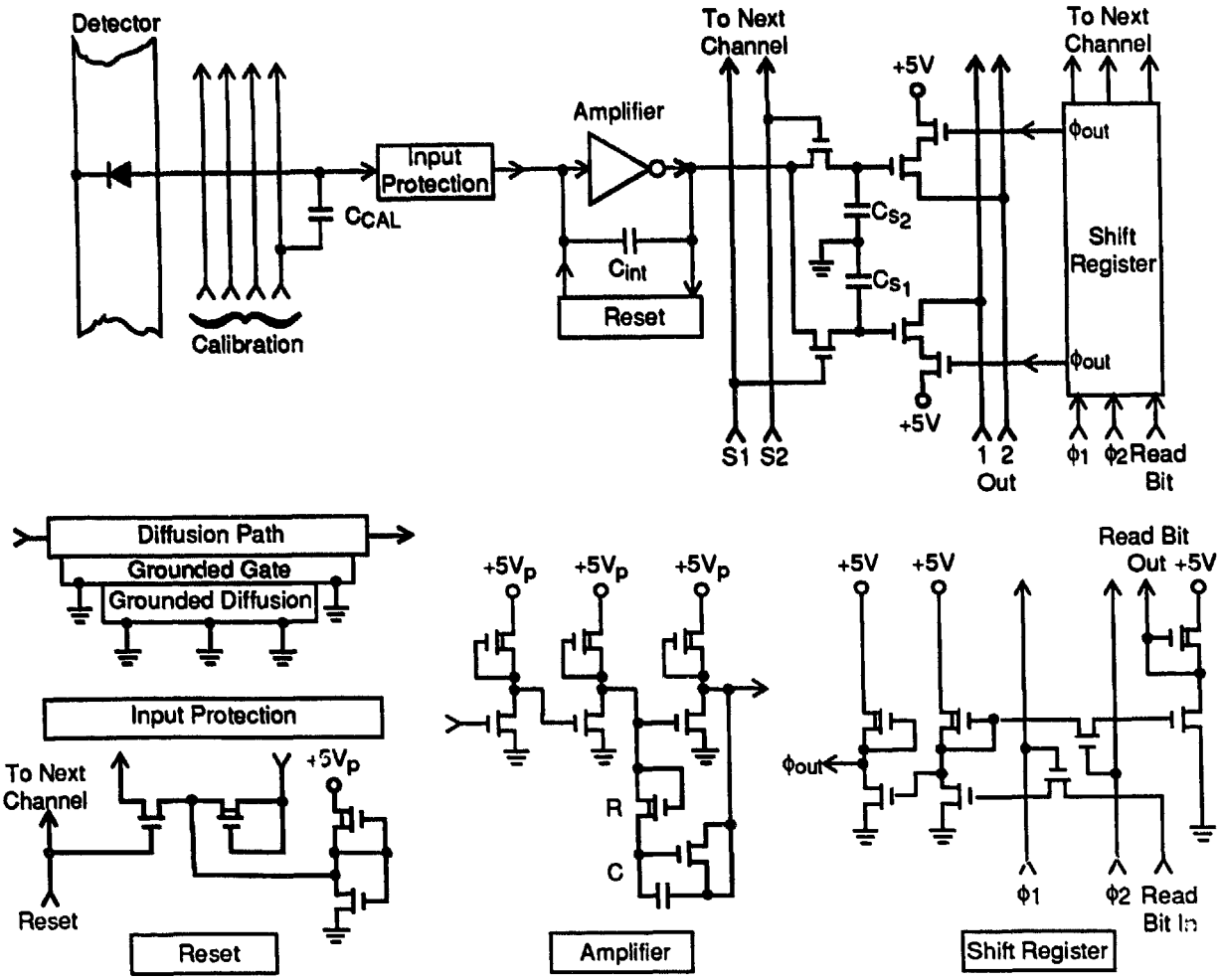

Fig. 7. Block diagram of a single channel of the Microplex circuit, plus schematics of the principal components, the Input Protection, the Reset, the Amplifier, and the Shift Register.

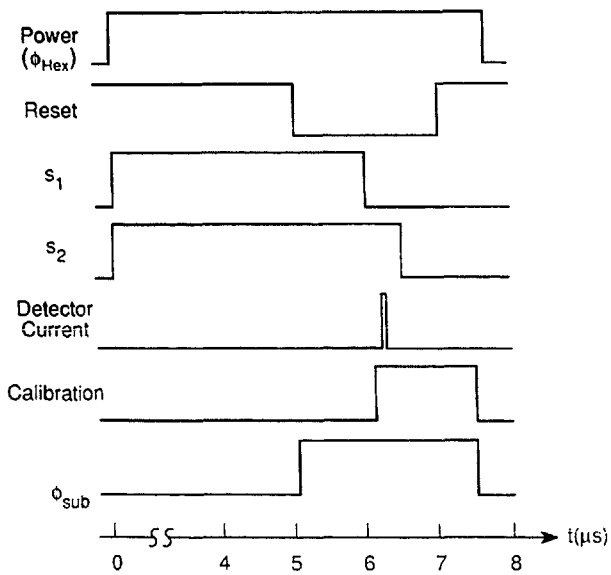

Fig. 8. Timing sequence for the operation of the analog section of the Microplex chip.

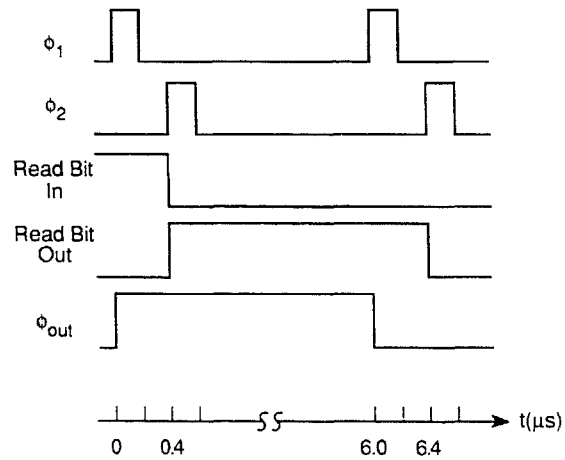

Fig. 9. Timing sequence for the operation of the digital section of the Microplex chip.

1–2 mm length, as were connections on the opposite side of the chips to power and control lines (the substrate voltage was connected to the bottom surface of the chips by conductive epoxy). The pads for the wire bond connections were 100 μm × 150 μm and were arranged on the input side of the chip in four rows of 32 (47.5 μm pitch) to match the pattern on the detector. Except for the wire bond pad areas, the chips were covered with a silicon nitride scratch mask for protection.

Besides the directly coupled signal input lines from the detector strips, there were four calibration lines on the Microplex chip that coupled capacitively (C_{cal} = 0.01 pF) to the input traces. Each line was connected to every fourth channel so that channel-to-channel cross talk could be measured. A calibration pulse of typically 0.5 V with timing as shown in fig. 8 was applied for testing. This yielded a signal approximately equal to that from the most probable charge deposited by a minimum-ionizing particle crossing the silicon detector. Input protection for the integrating amplifier was provided by a diode which shorted negative signals to the substrate, and a normally grounded-gate transistor which shorted large positive signals. All input control lines were protected in a similar way.

Charge integration was achieved with a three stage inverting amplifier with capacitive feedback (C_{int} = 0.1 pF). The open loop gain of the amplifier was roughly 400 which yielded an effective input capacitance of about 40 pF. The typical input capacitance from the silicon detectors was 10 pF, so about 80% of the charge produced in the detectors was collected on C_{int}. The amplifier dissipated 14 mW of heat per channel which necessitated limiting the duty cycle of its operation. At the SLC, the amplifier was powered for 7.6 μs per beam crossing which occurred at 120 Hz. The digital readout part of the chip was not powered during this time. To set the operating point of the amplifier, a FET switch which coupled the input and output of the amplifier was kept closed with the Reset pulse for 5 μs after power was applied.

The amplifier was stabilized against oscillation by an RC feedback network between its second and third stage which rolled off the high frequency response in a region where the feedback to the first stage became positive. The stability was aided by the voltage divider formed by C_{int} and the total input capacitance. To prevent oscillations during reset, a comparable voltage reduction occurred in the reset mode. This was achieved by connecting the amplifier output though a high impedance to both a low impedance voltage source and the amplifier input via the reset transistor. The voltage source was similar to the gain stages of the amplifier but with internal feedback so its output voltage was approximately equal to that of the operating point of the amplifier.

For our application, the integration period S_2–S_1 was set to 500 ns and centered about the expected arrival time of the signal from the silicon detector. This interval was much longer than the collection time of the charge produced within the silicon detector (≅ 30 ns), and also longer than needed by the rise time of the amplifier (≅ 25 ns). However, this choice of integration period alleviated the need for a very precise timing and did not significantly increase the output noise.

The storage capacitors C_{S1} and C_{S2} could in principle hold the amplifier induced charge up to about 50 ms before a significant degradation of the final signal would occur. In practice, the readout occurred only a few ms after the analog processing. The clock pulses (ϕ_1 and ϕ_2) which sequentially connected each channel to the output bus were spaced by 6 μs to allow the voltages to stabilize and the digitizer to process the signal. The Read Bit was daisy-chained between the four chips on a detector module so it took about 3 ms to read out an entire module. The digital section of the circuit dissipated 0.63 mW per channel during this period.

3.3. Performance tests

The Microplex chips were received in wafer form from the manufacturer and cut into chips following some spot checks. Each of the chips was then tested on a probe station using a computer controlled data acquisition system. For each channel, the response to a fixed calibration pulse, the rms noise, and the mean pedestal

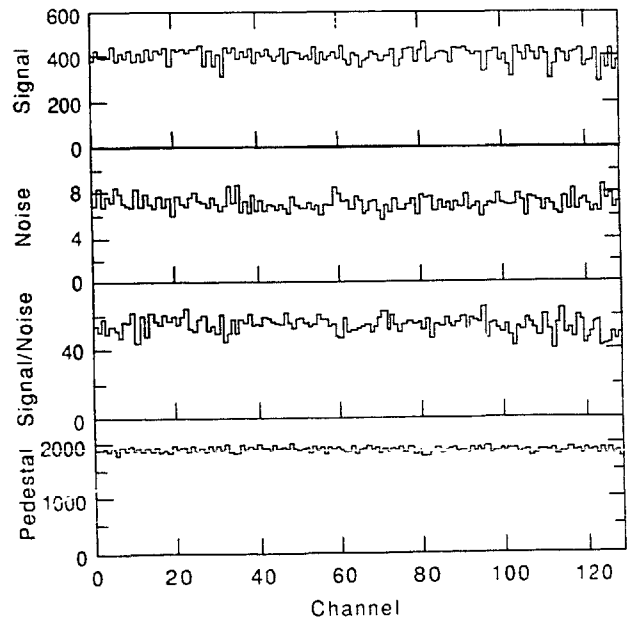

Fig. 10. Results of a pulser test for a given Microplex chip: The histograms show (averaged over 100 pulses) for each of the 128 channels (a) the signal (calibration response), (b) the rms noise, (c) the signal-to-noise ratio and (d) the pedestal in units of ADC counts.

were measured. Fig. 10 shows the results of a pulser test, including the ratio of the calibration response to rms noise, for a "good" chip. Chips that had one or more channels that deviated by more than 40% from the chip average in the calibration response, rms noise, or their ratio, were rejected for use in the SSVD. Chips were also rejected if any pedestal varied from the chip average by more than the size of the calibration response. The chip-to-chip variation of the average calibration response and rms noise was small (< 15%), so no cut was made on the absolute values of these quantities. On average, about 50% of the chips passed these very stringent selection criteria.

For a few of the Microplex circuits, the equivalent noise charge (ENC) was measured as a function of the input capacitance. Fig. 11 shows an example of such a measurement which was done by wire bonding surface mount capacitors of various sizes to some of the input pads of a chip. The data have a normalization uncertainty of about 10%. For a typical input capacitance of the silicon detectors of 10 pF, the ENC measurements predict an rms noise of 1250 electrons. This is in good agreement with signal-to-noise measurements made using both an X-ray source and minimum-ionizing particles (see sections 4.4 and 9.1). It should also be noted that the measured noise spectrum adhered very well to a Gaussian distribution. This was verified for a few detectors to the limit of statistics at five standard deviations. The spectrum is believed to be dominated by the thermal noise in the FETs of the integrating amplifier, primarily in the first stage.

3.4. Radiation hardness

The radiation hardness of the Microplex chip was a concern because of the closeness of the SSVD to the SLC beams. Potentially high radiation levels were expected from synchrotron photons and secondary particles generated by beam losses. This prompted a number of studies of the performance of the chips following exposure to ionizing radiation [14].

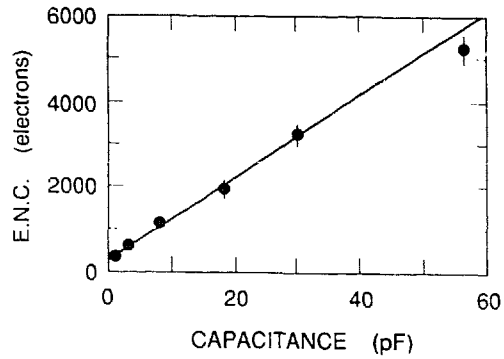

Fig. 11. Equivalent noise charge (ENC) of the Microplex chip as a function of external input capacitance. The line fit to the data has an intercept of 280 electrons and a slope of 97 electrons/pF.

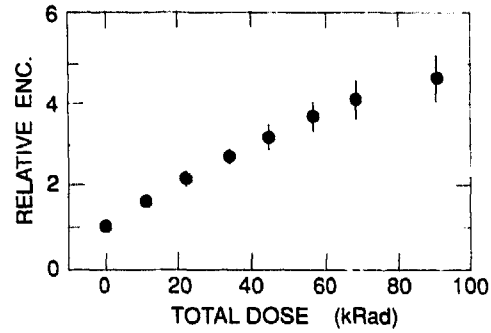

Fig. 12. Equivalent noise charge (ENC) of the Microplex chip as a function of radiation dose. The data are normalized to the ENC before exposure.

For this purpose, a few Microplex chips were exposed to a ^{60}Co source up to radiation levels of 100 krad. A nearly linear increase of the ENC with radiation dose was observed. This feature is shown in fig. 12 for a Microplex chip which was not wirebonded to a detector. The chip was not powered during the exposure although measurements with the power on at a 25% duty cycle gave fairly similar results. To interpret these measurements, one should note that a signal-to-noise reduction of roughly a factor of two was expected to significantly degrade the detection efficiency of the SSVD modules. Thus the circuits were expected to operate efficiently for radiation doses up to about 20 krad. This was verified for a fully assembled silicon detector module exposed to the ^{60}Co source.

Another effect of the radiation was a change in the turn-on thresholds of the FETs. This effect was measured with test structures which were irradiated along with the Microplex chips. The threshold changes resulted in a shift of the operating point of the integrating amplifiers of the Microplex circuit. As the threshold changes increased, the amplifiers were eventually driven into saturation. The shift in operating point could be compensated by pulsing the substrate by a few tenths of a volt just after the Reset switch was opened (ϕ_{sub} in fig. 8). In practice, this was only necessary for exposures above about 15 krad. To be safe, provisions were made that permitted the substrates of the chips of each detector module to be pulsed [15]. Also, the control electronics were designed to allow for a baseline adjustment of the timing pulses, and the control of the voltage level of the output bus. However, none of these options were utilized during the course of the run, nor was there any indication of a significant decrease in the signal-to-noise level (see section 8.2). This was consistent with the low level of exposure ($\approx$ 100 rad) measured by thermoluminescent dosimeters attached to the SSVD support structure.

4. The detector modules

4.1. Layout of the detector modules

The silicon strip vertex detector was composed of 36 detector modules which were designed to operate as independent units with their own power supply and readout. An exploded view of a module is shown in fig. 13. Each module consisted of a silicon strip detector and hybrid circuits at each end, H1 and H2. Each detector had 512 strips that were wirebonded to two pairs of Microplex readout chips. A laminated flat cable, placed under the hybrids and the detector, connected control, timing, and calibration signals, power lines, and the multiplexed output signal between the two hybrids and to the external control circuits. By connecting all input and output lines to a single multilead cable, the risk of generating potentially troublesome ground loops was reduced. At the same time, this configuration simplified not only the insertion of individual modules into the support structure, but also the installation of the completed device into the Mark II detector. The thin cable was connected to the ends of the hybrid circuits via aluminium wire bonds. At both ends of the module, the thin cable was sandwiched between the bottom of the ceramic hybrid and an insulated 200 μm thick stainless steel plate. These thin stainless steel supports had two functions. They stiffened and thereby protected the section of the thin cable that carried the wire bonds, and they provided a smooth reference surface for the placement of the module in the support structure. The silicon detector was epoxied to the surface of the hybrids and formed the mechanical connection between the two ends. On both hybrids, fanout circuits routed the control, signal and power lines to the two Microplex chips. A pair of precision machined brass fixtures was mounted on the insulated surfaces of the fanout circuits. They were designed to hold the module in the end-plates of the support structure. On the H2 side, the far end of the steel support was shaped to form a small hook for insertion.

At normal incidence, a particle traversed per layer a total of 5.0×10^{-3} radiation lengths, of which 3.4×10^{-3} was silicon. The remaining 1.6×10^{-3} was from the material of the cable, i.e., copper, Kapton [16], and epoxy, of which copper constituted 0.8×10^{-3} radiation lengths.

4.2. Design of the hybrid circuits

The ceramic hybrid circuits, H1 and H2, routed the control, calibration, and power lines from the thin cable to the two Microplex chips on each side. In

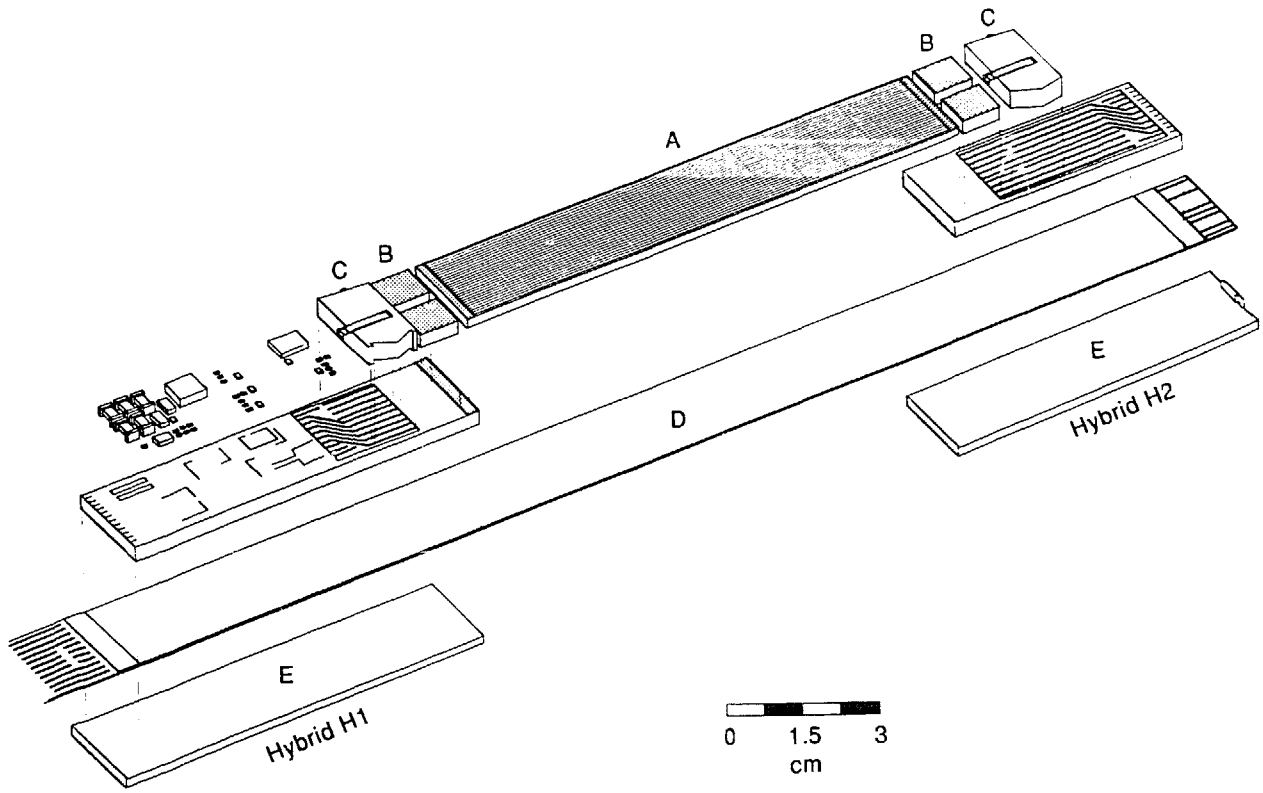

Fig. 13. Exploded view of a detector module showing the elements of the hybrids H1 and H2: A – silicon strip detector, B – Microplex readout chips, C – spring blocks, D – thin cable, and E – steel supports.

addition, hybrid H2 connected the analog output of the Microplex chips to the thin cable. While the hybrid circuit H2 was completely passive, the circuit H1 carried a differential amplifier and line driver for the analog output signal and also contained a switchable capacitor bank to power the amplifier section of the Microplex chips. The circuit diagram is given in fig. 14. The analog output of the Microplex circuit was connected to a wideband differential voltage amplifier, NE592, with the gain set at 10. The negative voltage levels V_{x1} and V_{x2} controlled the operating point of the source follower FETs of the Microplex analog output circuit. The silicon diodes, D_1 and D_2, prevented turn-on of the substrate junction when the Microplex circuits were powered off. Emitter followers of unity gain drove the 35 m long 50 Ω coax signal cables.

A bank of four tantalum capacitors with a total value of 27 μF stored charge during the interval between beam crossings (each at least 8 ms) and supplied the amplifier section of the Microplex circuits with a current of about 0.4 A for the few μs of operation per beam crossing. The switching element was a high-power fast FET [17] which was triggered by the external pulse ϕ_{hex}. Provisions were made for pulsing the substrate voltage, V_{sub}, with the pulse ϕ_{sub}. Passive filters were inserted throughout the circuit to reduce noise. For simplicity, they were omitted in the figure.

At each stage of the design of the modules, special attention was given to preserve a solid, loop-free grounding scheme and to shield the detectors, amplifiers and cables from high frequency electromagnetic fields generated by the passing beams. The ground connection for each module was carried through the supply cable to the external electronics. The power and ground lines for the hybrid circuits H1 and H2 were connected through a single path. The individual modules were electrically insulated from the aluminium support structure by a thin kapton foil covering the backside of the stainless steel supports.

4.3. Assembly of the detector modules

The detector modules were assembled in several steps. All components were tested thoroughly prior to assembly, and the modules were inspected, checked for electrical continuity and shorts, and subjected to functional tests after the completion of each fabrication step to ensure the largest possible yield. This was of particular importance because some of the components were expensive and because all of these assembly steps

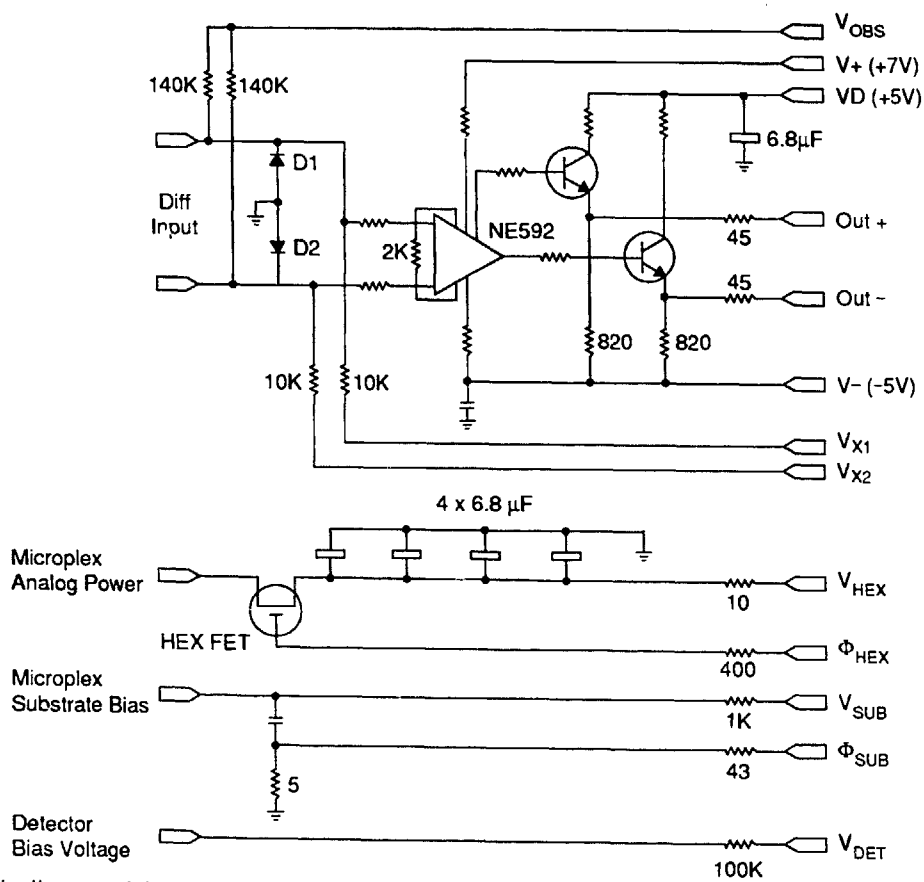

Fig. 14. Schematic diagram of the hybrid circuit H1. All resistors are quoted in Ω; all those unmarked have a value of 22 Ω.

involved epoxy joints or wire bonds and were therefore irreversible. In particular, the full operation of the amplifier circuits was tested prior to the attachment of the detector. As a result, only 3 of the 45 completed detector modules malfunctioned or had large numbers of failing channels. Apart from the size and fragility of the components that required extreme care and skill during the assembly, the sensitivity of the detectors to static charge build up on their surfaces caused problems. They were reduced by the introduction of air ionizers and the use of grounded floor mats and wrist bands.

The principal elements and their assembly steps were the following:

1) The H1 circuit was produced and assembled at a commercial hybrid firm [18] which also performed most of the wirebonding tasks. H1 consisted of a thick film hybrid with four conductive layers printed on a 375 μm thick ceramic substrate (Al_2O_3), with 250 μm line width and spacing. To convert the 500 μm line pitch on the hybrid to the 250 μm pitch of the Microplex bonding pads, fanouts were fabricated as double layer circuits printed on a thin kapton substrate (125 μm wide gold plated copper lines with 125 μm spacing). A pair of Microplex chips and a fan-out were glued to the ceramic substrate of both H1 and H2, and connected via aluminium wire bonds.

2) The thin flat cable connecting the two hybrid circuits was manufactured on 50 μm thick Kapton substrate [19]. A solid layer of 4 μm of Cu served as a ground plane on one side, and 16 traces of 4 μm thick Cu with 500 μm pitch were etched on the other side. The portion of the thin Cu traces that were to extend beyond the active length of the detector were then plated with 15 μm of copper and 3 μm of high purity gold to allow for bonding. The signal side of the cable was covered with an insulating layer of Kapton backed with a 4 μm thick copper shield. The laminations were bonded by a flexible epoxy [20]. To assure that the individual cables remained insulated from each other, the cables were wrapped with a layer of 25 μm thick adhesive Kapton.

3) In a custom-designed assembly jig, the two hybrids were spaced so as to span the length of the

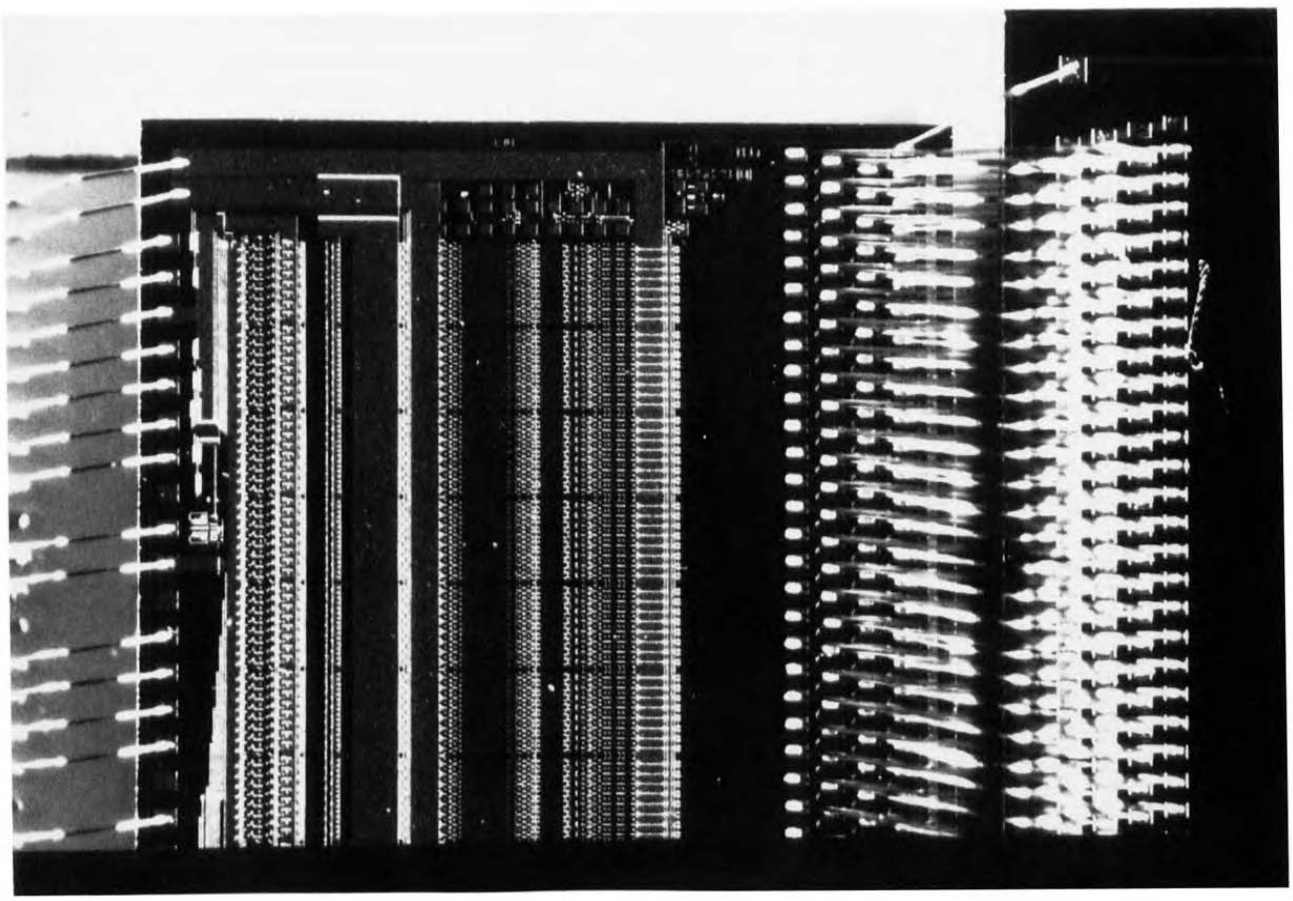

Fig. 15. Photograph of the Microplex chip showing the four layers of wire bonds connecting the detector (on the right) and a single layer of wire bonds connecting the hybrid (on the left).

silicon detector. The thin laminated cable was glued under pressure between the ceramic hybrids and the 200 μm thick stainless steel plates. Following one day of curing at room temperature, the hybrid circuits were wirebonded to the cable, and a connector was soldered to the end so that the assembled module could be electrically tested. After successful operation of the hybrid, the silicon detector was centered between the two hybrids using a micrometric vacuum manipulator and then glued to 1.5 mm wide edges on the ceramic substrates. For these structurally critical joints a high strength epoxy [21] was applied that cured at room temperature. On the H1 hybrid, a small amount of conductive epoxy [22] was added to assure electrical contact between the metallized backplane of the detector and the contact pad for the detector bias voltage. The mechanical strength of the resulting joint proved to be stronger than the silicon detector itself. The detector strips were then connected to the signal input pads of the Microplex chips. This was done on a manually operated ultrasonic wedge bonder using 25 μm diameter aluminium wires. The bond wires were arranged in four layers with the lowest connecting the closest pair of rows. No wire support was necessary, as illustrated in the photograph in fig. 15.

4) Following this step in the assembly process, the modules were once again submitted to a series of tests and calibrations. Upon successful completion the wire bonds were covered by a potting compound that cured at room temperature [23]. To increase its viscosity the compound was mixed two hours before application. Dams were set up to prevent the potting compound from spreading beyond the edges of the hybrid. The potting process embedded all wire bonds and substantially increased the rigidity of the module, thereby making it insensitive to damage by contact. On the other hand, the potting compound prevented access to all elements of the hybrid circuit. However, in a few cases, we were able to remove a small volume of the cured compound with a very fine tip of a hot soldering iron and perform repairs on the hybrid.

5) A precision jig was used to align a pair of brass spring fixtures relative to one of the edges of the silicon detector and to epoxy [24] them over the fan-outs on the hybrids. The traces on the fan-outs were insulated from the spring fixture by a 25 μm thick Kapton film.

6) The last assembly task was the replacement of the temporary connector at the end of the thin cable by a 137 cm long, copper shielded flat cable of identical width and signal line layout. Since no connector of appropriate dimensions was available, the two cables were fused. For this purpose the gold-plated signal traces on both cables were first coated with low temperature solder. The matching traces were then placed on top of each other and fused over a length of 5 mm to 10 mm by applying heat and pressure. The joints were subsequently reinforced on the outside with adhesive Kapton tape.

4.4. Performance tests

A series of tests was performed to compare and evaluate the performance of the assembled detector modules and to eliminate malfunctioning ones.

4.4.1. Pulser tests

The performance of individual Microplex chips as well as fully assembled detector modules was tested with a CAMAC controlled test pulser system. A pulse of adjustable amplitude was applied individually to each of the four calibration lines on the Microplex chips that were capacitively coupled to every fourth amplifier input. The charge was integrated and stored, and subsequently read out via a microprocessor controlled ADC into a computer. This procedure was designed to provide fast diagnostics and could, in principle, measure the gain of individual amplifiers. In practice, the size of the stray capacitance between the potted bond wires and the calibration lines turned out to be significant in comparison to the calibration capacitors. [#1] As a result, the injected calibration charge varied as much as 20% from channel to channel, depending on the orientation and spacing of the bond wires. However, the channel-to-channel variation was small enough to permit a functional test of the amplifiers. For this purpose the response of a single channel, S_i, was measured in units of its rms noise, N_i, and compared to the average response of all channels of a given module for a fixed pulser setting, namely $A = \langle S \rangle / \langle N \rangle$. The amplitude of the calibration pulse was adjusted to correspond to 24000 electrons, the most probable charge deposited by a minimum ionizing particle crossing the detector at normal incidence. Fig. 16 shows a typical record of the pulser test performed on a detector module. The output of a channel varied because of gain variations, noise, or high leakage current. A channel was classified as "bad" if its ratio $A_i = S_i/N_i$ differed significantly from the average of all channels in the module, specifically, if it did not satisfy the relation: $0.5 < A_i/A < 2.0$. There were a total of 257 bad channels detected for the 42 detector modules that were tested, corresponding to 1.2% of all channels. Fig. 17a shows the histogram of the number of "bad" channels per module.

[#1] The calibration capacitors were kept small so noise on the long calibration lines would not couple to the amplifier input.

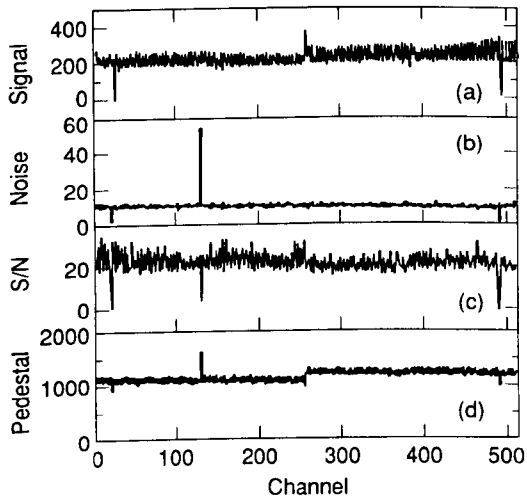

Fig. 16. Record of a typical pulser test of a completely assembled detector module. The following quantities, averaged over 100 pulses, are plotted in ADC units as a function of the channel number (511 active channels per module): (a) pedestal subtracted signal S_i; (b) rms noise N_i, (c) the ratio S_i / N_i, and (d) the pedestal. The noise is defined as the rms fluctuation of the pedestal.

4.4.2. Leakage current tests

The bulk leakage current for a fully depleted silicon detector is a simple measure of the quality of its performance. To burn in the components of the hybrid circuits and to test for possible breakdown of the detector diode structures, the detector modules were operated in the laboratory continuously for one week. During this time the detectors were held at a constant operating voltage and the leakage current was monitored. Typical leakage currents varied between 0.2 and 4 μA; the distribution of the measured currents is given in fig. 17b. Some modules drew a constant leakage current from the beginning to the end of the test, others showed a significant rise during the first day of operation and then reached a constant level.

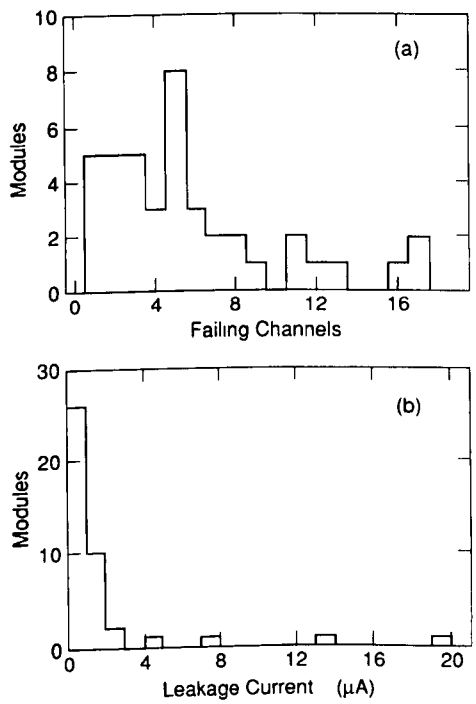

Fig. 17. Histogram for the 42 detector modules of (a) the number of failing channels and (b) the leakage currents measured after a week-long operation at full voltage.

During the week-long test, the calibration system was pulsed, and the detector was read out once per second. Data from the beginning and the end of the test were compared. Of the 45 modules that were tested, two developed an area of 10–20 adjacent bad strips. No increase in detector leakage current was observed that could be associated with this failure mode and its cause remains uncertain.

4.4.3. Signal-to-noise measurements

In the absence of a test beam of minimum ionizing particles, an ^{241}Am source of 250 mCi was used to measure the signal-to-noise ratio for the assembled detector modules and to measure channel-to-channel gain variations. Photons of 59.5 keV were emitted from the source and produced signals in a detector that corresponded to 71% of the most probable energy loss of a minimum ionizing particle. Since the absorption length of these photons in silicon was large (1.4 cm) compared to the detector thickness, the photons were absorbed uniformly throughout the detector. The photoelectrons produced had a range of less than 20 μm, so on average the spread of the collected charge was similar to that from a minimum ionizing particle traversing the detector. It was assumed that the absorbed photon spectrum was dominated by a single photon energy of 59.5 keV. This was a reasonable assumption given the lower intensity of the 14 and 18 keV lines and the fact that the detector was covered by the 0.8 mm thick aluminium lid of the carrying case.

With a gate width of 400 ns and a readout rate of 1 Hz, on average 20 photon interactions were recorded per minute, and a 15 hour run was necessary to collect 30–40 photons per strip for a given module. Pedestals were derived from data recorded without the source and the noise per channel, σ_i was taken as the rms width of the pedestal distribution. To find X-ray hits, a cluster finding algorithm was applied. A cluster required at least one strip with a pulse height above pedestal greater than $5\sigma_i$, and was defined as a group of three strips centered on the strip with the largest pulse height. A histogram of the total cluster pulse height is shown in fig. 18 for a single detector module. The pulse height is measured in units of the ADC [25].

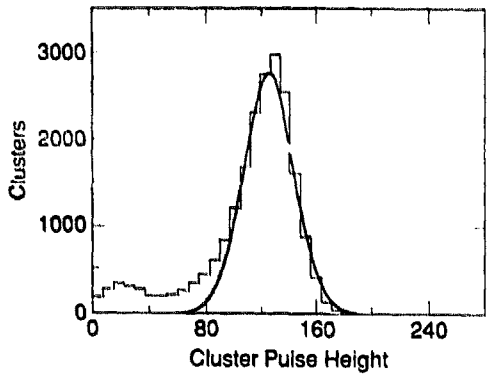

Fig. 18. Distribution of cluster pulse heights recorded by a silicon detector module exposed to an ^{241}Am source. The pulse heights are measured in ADC units. The curve represents a Gaussian resolution function fitted to the pulse height data above 100.

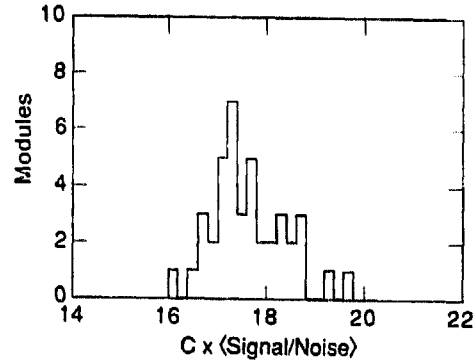

Fig. 19. Distribution of average signal-to-noise ratios for the detector modules, measured with an ^{241}Am source. The pulse-height scale has been adjusted to correspond to minimum ionizing particles, i.e. $C = 1/0.71$.

The Gaussian fit to the data does not include the low energy tail of the distribution. This tail resulted primarily from X-rays that were recorded near the edges of the amplifier integration period. The mean of the fitted curve is 128 which corresponds to a most probable energy loss for minimum ionizing particles of $128/0.71 = 180$, compared to the measured single channel rms noise of 9.4. Assuming that 3.6 eV are required to produce an electron–hole pair in silicon, the measured signal-to-noise ratio of $180/9.4 = 19.2$ translates to an equivalent noise charge of 1250 electrons, which is in agreement with the measurement in fig. 11 for an input capacitance of 8.8 pF (sum of strip-to-strip and strip-to-backplane capacitance for a detector of layer 1). The width of the pulse height distribution in fig. 18 is about 20% smaller than the naive expectation based on the sum of the noise of three independent channels. However, it is consistent with the observation of negative noise correlations at the level of 20% between neighboring channels which arise from capacitive coupling [26,27]. The distribution of the signal-to-noise ratios averaged over all strips per detector module is given in fig. 19. The mean value is 17.6 times the average single channel noise.

4.4.4. Gain measurements

The X-ray data were also used to measure channel-to-channel gain variation. For this purpose, the gains of all channels were adjusted in an iterative procedure to produce the same average pulse height for all clusters in a module, irrespective of their location. Special care was taken to avoid a bias caused by the low energy tail in the cluster pulse height distribution mentioned above. A histogram of the measured relative gain constants of all channels is presented in fig. 20, showing a spread of about 10%. For all channels of a given Microplex chip the gain varied typically by 1–2%. The relative gains remained stable over several months provided the supply voltages and currents were kept constant.

4.4.5. IR light source test

A narrowly focussed beam of infrared light was used to test the response of the detectors locally. This test also checked for shorts, open connections, or incorrect connections between the detector strips and the amplifier circuits. For this purpose, a detector module was placed on a translation stage and moved under computer control with an accuracy of 1 μm relative to a fixed IR light spot. To generate a light spot with a diameter of 5 μm on the detector surface, a light emitting diode [28] was mounted in place of one of the eye pieces of a microscope [29]. The infrared diode was dc operated and its intensity was adjusted so that the deposited charge was comparable to that from a minimum ionizing particle. The infrared photons had a wavelength of 850 nm and penetrated roughly 20 μm into the silicon, but they were absorbed in the 8 μm wide, 0.5 μm thick aluminium readout strips covering the strip diodes. Fig. 21 shows an example of a scan with the IR light source. A normally functioning readout strip shows a doubly peaked intensity profile because of the aluminium strips on the detector surface.

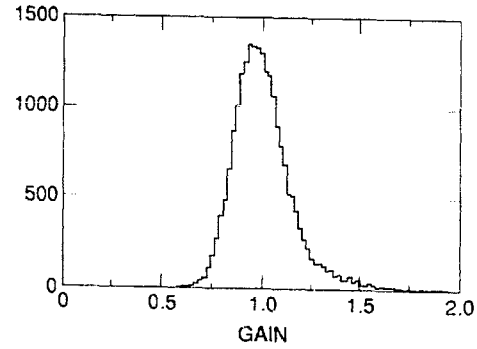

Fig. 20. Histogram of the relative gains of all detector channels.

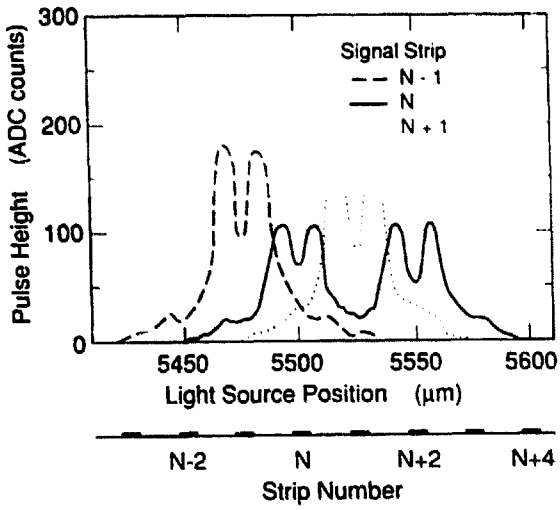

Fig. 21. Example of an IR light source scan illustrating the detection of two electrically connected strips on a prototype detector module: the measured pulse height for a given readout strip (measured in ADC units) is shown as a function of the transverse position of the light spot for three adjacent strips. Strips N and $N+2$ are electrically shorted. They are adjacent readout channels and thus have adjacent wire bonds.

Electrically shorted strips are evidenced by the fact that half the normal pulse height is recorded on channel N with the source centered on either channel N or $N+2$. Scans of assembled modules were primarily used to check for errors or shorts at the wire bonds between the detector and the Microplex input pads that could easily be corrected before the potting process. Following a correction of the chip alignment during the assembly procedure, no shorts or bonding errors were discovered.

5. Electronics and data acquisition

A block diagram of the electronics system which controlled the operation of the silicon detector modules (SDM) and processed their output signals is shown in fig. 22. This system resided in the electronics support building for the Mark II detector. Each of the 36 SDMs was connected through a multilead coax cable to one of nine driver/receiver modules, four SDMs per receiver. These modules converted pulses from the analog timing module to pulses of appropriate amplitude and source impedance for the operation of the SDM hybrid and Microplex circuits. These timing pulses controlled the operation of the analog section of the Microplex. The multiplexing of the analog data was controlled by pulses from the BADC, a microprocessor driven ADC [25]. The driver/receiver modules also routed and generated dc voltage levels for the SDM operation, and contained line receivers for their analog output signals. The line receiver output from each driver/receiver module was connected to the analog input of the BADC. Each BADC processed the analog data from four SDMs and stored the results in its digital memory. All nine BADCs operated in parallel and upon completion of the digitization and processing, the data were read out sequentially by the Mark II data acquisition system. The system also monitored the bias voltages and leakage currents of the silicon detectors, and some of the control voltages for the SDMs. A more detailed description of the components of the SSVD data acquisition system follows.

5.1. Cables

The 1.4 m long flexible cables described in section 4.3 brought the 25 lines from each SDM to the endcap of the Mark II detector. These lines were extended to the driver/receiver modules by a 35 m long ribbon coax cable. The flexible cables were individually wrapped in an electrical shielding material that was insulated from their ground planes. One end of the shielding connected to the module housing, and the other to the grounds of the coax cable.

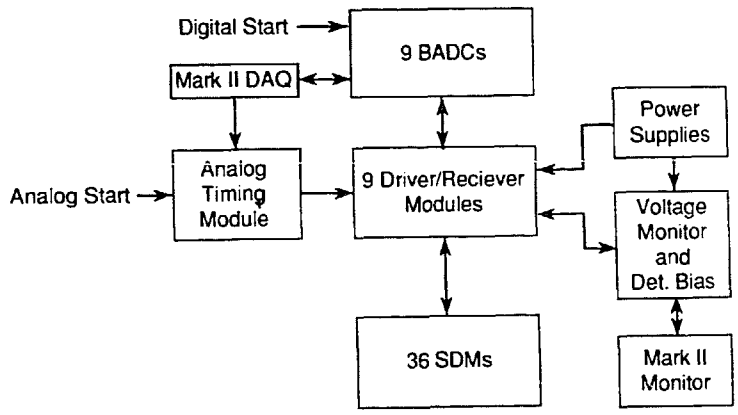

Fig. 22. Block diagram of the data acquisition system for the SSVD.

5.2. Analog timing module

This module generated the timing signals shown in fig. 8 for the analog operation of the Microplex chip. The timing of the pulses was achieved with clock count timers which were set by DIP switches. The timing sequence was initiated prior to the beam crossings. In addition to the timing pulses, four voltage levels were produced to control the amplitudes of the four calibration pulses generated in the driver/receiver modules. These voltages were set under computer control (this was the only programmable feature of the module).

5.3. Driver/receiver modules

The main components of these modules were line drivers for the timing pulses. The drivers were designed to allow flexibility in the operation of the SDMs: the output pulses were back-terminated, had adjustable amplitudes and baselines, and were shaped so their rise times at the SDM end were sufficiently short (< 50 ns to reach 90% of the maximum amplitude for the critical timing pulses). Potentiometers permitted the adjustment of the baselines of most of the pulses so as to counteract threshold shifts expected as a result of exposure to ionizing radiation. The pulse amplitudes were under control by common external reference voltages, except for the amplitude of the substrate pulse which could be set individually for each module, and the power switch controller (ϕ_{hex}) amplitude which was fixed. The dc levels, V_{sub}, V_{x1} and V_{x2}, were also controlled by individual potentiometers. However, only one of the almost 230 individual controls had to be adjusted during the course of the Mark II run.

Another function of the driver/receiver module was to convert the timing pulses from the BADC to the ones required for the Microplex chip readout (ϕ_1, ϕ_2, Read Bit). During the sequential readout of four SDMs by one BADC, only one SDM was powered at a time in order to minimize the power dissipation. The power switching was performed in the driver/receiver module and controlled by two Module Select lines from the BADC. The analog signals from each set of four SDMs were connected to a differential receiver in the driver/receiver module. The receiver outputs were ORed and sent via a baseline shifter to the analog input of the BADC.

5.4. Voltage monitor and detector bias supply module

To monitor the detector bias voltages, detector leakage currents, and various control voltages, it was convenient to combine the monitoring and detector bias supply system in a single module. From this module, multiconductor cables were connected to each of the driver/receiver modules to supply the detector bias voltages and receive the voltages to be monitored. The bias voltage for each SDM could be adjusted by a potentiometer. The currents drawn by the detectors were monitored using a current-to-voltage converter. The voltages monitored in the driver/receiver modules included V_{sub}, the substrate voltage, and V_{x1} and V_{x2}, two levels which controlled the baseline of the output pulses. The power and reference voltages that were bused to all driver/receiver modules were also recorded.

A custom CAMAC module was built to multiplex the voltages to a digitizer and then store the results in an internal memory. The digitization was initiated and the data were read by the Mark II monitor system every 4 min. The 260 measured voltages were compared to their allowed range, and the system alerted the operators of the experiment if any value exceeded the specified range.

5.5. BADC readout

The SSVD was read out via microprocessor-controlled ADCs that were custom-built for the Mark II experiment in 1977 [25]. These so-called BADCs controlled the analog multiplexing of the Microplex signals, digitized the signals, and executed programmed algorithms for data correction and sparsification. The BADCs were modified for this application: their program memory space was doubled to 512 48-bit words, their instruction rate was lowered to 20 MHz, and digital control signals were sent to the driver/receiver modules. The data were processed in two passes. During the first pass, the data were acquired from the Microplex chips in a pipeline operation, they were digitized and preprocessed, and then stored in order of strip numbers for each detector. This first pass was essentially identical for both calibration and normal data taking. During the second pass corrections were applied for common pulse height shifts, pedestals were updated, and the data were compressed, reformatted to contain the strip addresses, and subsequently stored in an output buffer.

Upon receipt of the start pulse from the trigger logic, all BADCs began processing data in parallel. For each channel, the BADC digitized the pulse height S_i, subtracted the pedestal P_i, and stored the differences, $D_i = S_i - P_i$, in order of strip number. For channels that were not flagged as bad and had a pulse height with $|D_i| < 255$, the values of D_i were summed. For each Microplex chip this sum was divided by the number of channels included in the sum, $C_m = \Sigma D_i/N$, and the result was recorded and taken as an estimate of a pulse height shift common to all channels. Under normal conditions, these so-called common mode shifts were negligible, though at times they exceeded the

noise level significantly, and thus by taking their effect into account, the signal pulse heights could be corrected online.

During the second pass through the data, a cluster finding algorithm was used to select and store channels with significant pulse height information for transfer to tape. For this purpose, a running sum of common mode corrected pulse heights of three adjacent strips, $R_i = \sum_{i-1}^{i+1}(D_i - C_m)$, was compared to the sum of thresholds, $X_i = \sum_{i-1}^{i+1} T_i$, for those same strips. If $|R_i| > X_i$, channels $i-2$ to $i+2$ were selected and their pulse heights $D_i - C_m$ were stored for readout. Special care was taken to assure that each strip was read out only once.

Pedestals for all channels were updated on an event-by-event basis using a moving average algorithm with an exponential averaging filter, $P_i^{k+1} = P_i^k + D_i/32$. Here the pulse heights were not common mode corrected so that common pedestal drifts could be taken into account. The pedestals were not updated for bad channels (typically 85 strips) and for channels selected for readout by the cluster algorithm (on average 1% of all strips) in a given event. Due to the limited number of bits available in the BADC, the filter used only 4 bits for the fractional part of the average; this had no discernable effect on the data.

The threshold values were set to $T_i = 2.0\ \sigma_i$, where σ_i was the rms noise of a single strip. This threshold corresponded to about 34% of the most probable signal expected for a minimum ionizing particle at normal incidence. In terms of the width of the noise distribution for the three-channel running sum, the threshold was placed at $6.0/(0.8\sqrt{3}) = 4.3$ standard deviations. Here, the factor of 0.8 accounts for noise correlations between adjacent channels.

In order to adjust to the rather long rise time of the signals at the output of the driver/receiver module, the readout was slowed down from a maximum rate of 1 μs/strip to 6.2 μs/strip, resulting in a processing time of 13 ms for the first pass. The second pass took on average an additional 6 ms; the exact time depended on the number of clusters found. The sequential transfer of data from the nine BADCs to the VAX on-line computer added on average 1.3 ms to the total readout time.

Approximately once every eight hours, the data acquisition system was operated in calibration mode. Calibration pulses of different amplitudes were sent to the SDMs, and the pulse heights were recorded by the BADCs using the same timing sequence as during data taking. The BADCs accumulated the means and variances of the pulse heights and transferred the data to the on-line VAX computer. Gains for individual channels were calculated and recorded together with the pedestals and rms noise. The results were compared to data from previous calibrations, and cuts were placed on the size and linearity of the gain, as well as the size of the rms noise and pedestals. Failing channels were logged and brought to the operator's attention. Channels that failed repeatedly were marked as bad and suppressed in subsequent BADC readout. Measured pedestals and thresholds were updated in the BADC database for subsequent use. The pulser calibration was not used for setting the channel-to-channel gain correction, because of the variation of the effective calibration capacitors on the Microplex chip (see section 4.4). Instead, gain corrections measured with the ^{241}Am source prior to installation were applied off-line.

6. Mechanical support and placement of modules

The excellent spatial resolution of the silicon strip detectors placed stringent demands on the precision, alignment, and rigidity of the support structure. The concept adopted here was to place the detectors to a moderate accuracy of about 50 μm and to use precise alignment techniques to determine their relative location to the level of 2 μm. The placement tolerance was set so that the 2 mm uncertainty in the extrapolated track position along the z axis would not significantly worsen the $r\phi$ measurement by the silicon detector. This meant that the silicon strip detectors had to be placed to within 1 mrad parallel to the axis of the overall coordinate system defined by the central drift chamber.

6.1 Support structure

To allow for easy installation on the vacuum pipe, the support structure was made of two identical halves. Each half was placed on the central section of the vacuum pipe using a three point mount, and held in position by flat copper springs. The points of contact were three sapphire balls, 3 mm in diameter, that assured that the support was electrically insulated from the vacuum pipe. One of the two hemicylindrical structures built to support the detector modules is shown in fig. 23. The detector modules were inserted into slots of two aluminium end pieces which were connected by two half-cylindrical beryllium shells of 250 μm thickness. The end pieces were fabricated by electrodischarge machining. The two matching ends were cut simultaneously out of one block of aluminium so as to obtain an accurate match of the slots at the two ends. We verified that the dimensions of the slots were accurate to about 10 μm, their relative location in a given layer was measured to agree with the design to an accuracy of 11 μm in radius and 0.6 mrad in azimuth. The thin inner beryllium shells and the 1 mm thick aluminium extensions were epoxied to the inner rims of the end pieces. The assembled holders showed

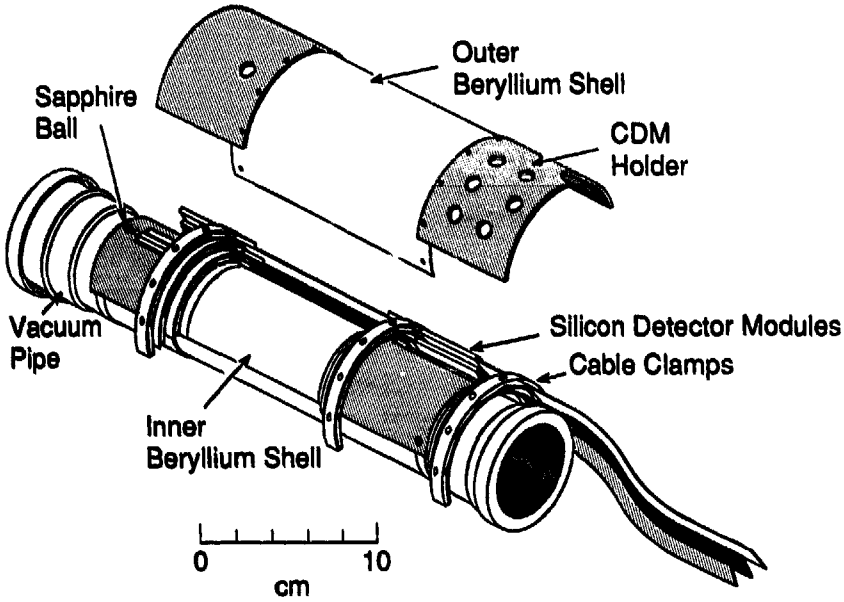

Fig. 23. Sketch of one of the hemicylindrical support structures with a few sample detectors inserted into the slotted end pieces. The flat cables are secured by a cable clamp attached to the vacuum pipe.

relative azimuthal offsets of the slots in the two pairs of end pieces of 0.3 mrad and 1.0 mrad. The outer beryllium shell was designed to be attached with screws to the outer rim of the end pieces, after the detector modules had been inserted.

6.2. *Spring fixtures*

Once inserted into the slots, the modules were held in place by spring-loaded fixtures which were epoxied to each end of the modules. These fixtures were designed to place the modules to an accuracy of about 50 μm and to maintain their position to 2 μm. Fig. 24 shows one of the spring fixtures which were assembled from three components;

- a spring block, cut by wire electrodischarge machining from a 1 mm thick sheet of brass,
- a wire spring, made of 0.4 mm diameter phosphorous bronze, and
- a cover with a vertical spring, cut and shaped from a sheet of 125 μm thick beryllium–copper.

The wire spring was inserted into the cavity of the spring block and compressed by roughly 200 g. The cover was spot welded on to the spring block. The wire spring pushed the module against one side of the slot that acted as the reference surface for its azimuthal location. The vertical spring pressed the module against the bottom of the slot and thereby determined its radial location. The height of the vertical spring was adjusted so that its force did not impede the action of the horizontal spring. The spring blocks for the three detector sizes differed only in the total width. They were made in pairs: at one end, the spring block design allowed the modules to move parallel to the detector strips, and at the other end (the cable end), the spring block captured the endplate to prevent the module from being pulled out accidentally.

To assure the desired parallelism between the detector strips and the holder axis, a special jig was built to precisely place the spring blocks relative to the detector strips. A pair of spring blocks on a given module had to be aligned to within 0.05 mm. Since it had been verified that the detector edges were parallel to the detector readout strips to within 0.2 mrad (see section 2.2), these edges were used as reference. With

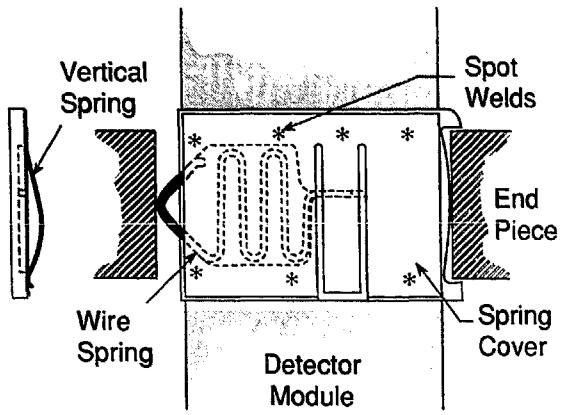

Fig. 24. Top and side views of the spring block for the cable end of the module, detailing the wire spring for horizontal placement, and the cover with the flat vertical spring for radial placement of the modules in the slots.

the exception of two modules, the pairs of springs blocks were found to be parallel to the detector strips to better than 0.5 mrad.

A series of tests was performed to examine the stability and accuracy of the module placement. The design performance was verified. Furthermore, a number of tests showed that the modules retained their placement and shape after the room temperature had been cycled by up to 15°C over periods of 30 min or more.

6.3. Cable clamp

It was observed that motion of the cable attached to the module could substantially change the placement and shape of the detector inserted in the slotted end pieces. Therefore a clamp was built to hold each cable in a thin slot that was aligned with the slot in the holder (see fig. 23). The cable clamp was attached to the vacuum pipe with nylon screws. While the cable clamp provided strain relief for individual cables, the assembly of 18 cables attached to the clamp introduced an undesirable constraint of the support structure.

6.4. Rf shielding

To avoid interference from high frequency electromagnetic fields generated by passing beams or the surrounding electronics of the Mark II detector, special care was taken to electrically insulate the detector modules from the aluminium support structure, as well as the support structure and cable clamp from the vacuum pipe. The detector modules were completely enclosed by metal shielding: the beryllium shells and the end pieces were attached to a flexible cable shield made of 25 μm thick aluminium laminated with Kapton on both sides. The shield enclosed the open ends of the support structure, and it extended over the full length of the 1.4 m long cables.

7. Alignment techniques

7.1. Introduction

Although the module housing described in the previous section placed the detectors to an accuracy of about 50 μm, a much better knowledge of their location was needed to exploit the intrinsic resolution of about 5 μm for particle tracking. The simplest approach to determining the alignment of the detectors would have been to minimize the distances between hits in the SSVD and tracks reconstructed in the drift chambers of the Mark II. This method would have required a large number of tracks, preferentially of high momentum and distributed more or less evenly over the detector. It would also have required a zeroth order knowledge of the location of the individual detector modules, and the results would have been sensitive to the systematic errors in the projected track positions which were expected to be substantially larger than the intrinsic resolution of the silicon detectors. To try to avoid this problem, two methods were developed with the goal of precisely measuring the internal alignment of the detectors in each half of the SSVD before it was installed in the Mark II. The global alignment of each half with respect to the other tracking detectors would then be established using tracks recorded during the Mark II run. In this procedure, local systematic errors in the drift chamber track reconstruction would tend to be averaged out. Motion of the vacuum pipe, and hence the SSVD, relative to the drift chambers would be measured and corrected for by using the capacitive displacement measuring (CDM) system.

Because the strip spacing on the detectors was precisely known, the internal alignment problem was reduced to one of finding the relative positions and orientations of the 18 detectors in each half of the SSVD. This problem was formulated in terms of misalignments in position and angle of the detectors relative to their nominal settings in the detector housing. To see how these misalignments were specified, consider a single planar detector in a reference frame where its strips are parallel to the z axis and perpendicular to the x axis as shown in fig. 25. Let the detector be nominally centered about $x = z = 0$ but displaced vertically to represent its radial position in the module housing. From this nominal setting, the translational displacements Δx and Δy of the center of the detector, and the rotational angles α_y, α_x and α_z were chosen to represent the alignment degrees of freedom. This choice insured that these parameters

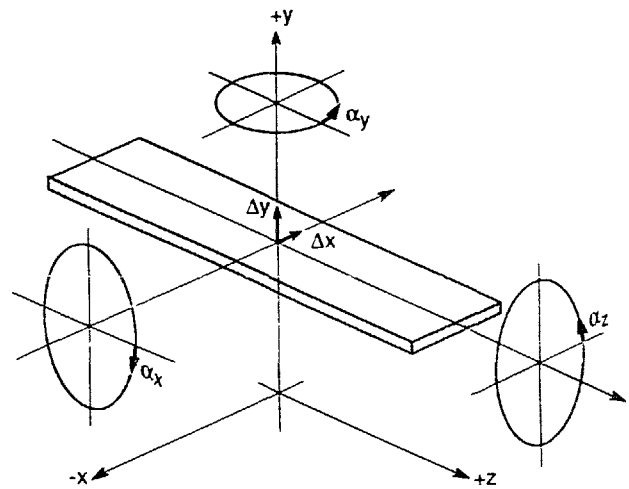

Fig. 25. Definition of the parameters describing the position of the single silicon detector relative to its nominal position. The detector strips run parallel to the z axis.

would be small so a first order approximation could be used in the alignment computations. In practice, it was found that some of the detectors acquired a significant bow and twist when installed in the support structure. To account for this, an additional vertical displacement of $Az^2 + Bxz$ was included in the parameterization where the value of A represented the bow and B the twist. In all, seven parameters were used to specify the x and y positions of the detector strips at any z location.

The two techniques developed to measure these parameters took somewhat orthogonal approaches to the problem and thus provided means of cross checking the results. Both surveys were performed in the temperature stabilized laboratory at 29°C, the same temperature that was expected for operation of the SSVD inside the Mark II. The first method was an optical survey of the detectors. The positions of a few reference strips on the detectors were recorded with an optical measuring microscope after each layer was inserted into the support structure. During this process, the outer shells of the half cylinders were not attached so that the detector strips could be viewed. In the second alignment procedure, the SSVD was moved through a fixed X-ray beam using a set of precision stages [30]. The beam positions reconstructed from the detected signals together with the stage settings were then used to compute the detector alignment. The advantage of this method was that the beam penetrated the shells and the detectors so the measurements could be made after the assembly was complete.

7.2. Optical alignment

During the installation of the detector modules into each of the hemicylindrical support structures a 3-dimensional measuring microscope [31] was used to survey the location of individual detectors. During this operation the SSVD support structure was attached to a replica of the vacuum pipe which was mounted horizontally on a rotation stage. The rotation stage was in turn mounted on the orthogonal linear stages of the microscope. The stages and the focus of the microscope were operated manually, and the coordinates were read out via an RS-232 port into a computer. The survey relied heavily on a set of fiducials to relate measurements taken at different settings of the rotation stage. For fiducials we used tips of micropositioner probe pins [32], 0.6 and 1.2 μm in diameter. Six pins, spaced by approximately 30° in azimuth, were epoxied to each of the outer rims of the two end pieces of the support structure. Each pin was visible over a range of stage angles of ±30°, so at any stage position there were at least four, and normally six, measurable fiducials.

Prior to all measurements the microscope was calibrated and the orthogonality of three axes was checked. As in fig. 25, the z axis was defined to be parallel to the axis of the vacuum pipe, the y axis was vertical, and the x axis was transverse to the other two axes. For calibration purposes, the positions of the fiducials were measured over a wide range of stage angles, and the non-orthogonality of the three microscope axes was determined by requiring that the distances between any pair of fiducials be independent of their orientation. The scale and the direction of the z axis were taken as reference. The biggest correction found was for the angle between the y and z axes which was off by 4×10^{-4}. The relative scales in x and y were too small by 1.5×10^{-4}. All other corrections were within the tolerance of 1×10^{-4} given by the manufacturer. Subsequent coordinate measurements were corrected for the scale calibration and non-orthogonality of the axes. From repeated measurements of positions and distances rms errors for measurements in the x, y, and z directions of 0.8, 1.3, and 0.8 μm, respectively, were determined. For simplicity, a uniform error of 1 μm was assumed for all fiducial measurements in the subsequent analysis.

After insertion of the modules in a given layer, the six detectors were measured. For each detector, coordinates (x, y, z) on the surface were recorded at three stage settings: the angle at which the detector was horizontal, and at ±15°, i.e., angular settings at which the detector and one of its neighbors could be measured. For each stage setting, points were measured along each of the two outer diode strips, at roughly 10 mm intervals in z, and at a few positions close to the central strip on the detector. For each layer, 11–12 stage settings were necessary. The rotation stage was not assumed to be perfectly aligned and calibrated, but each set of measurements was transformed to a common reference frame relying on the set of fiducials that were measured concurrently with the detectors. Several different methods were used for these transformations, the results agreed very well within the estimated errors.

The measured orientation and position of each detector was compared to its nominal position in the support structure (see fig. 25). The placement was parameterized in terms of pitch, yaw, and roll angles, α_x, α_y, and α_z, and horizontal and vertical offsets, Δx and Δy. The z position was defined for all detectors to coincide with the center of the support structure. The shape was described in terms of A and B, the bow and twist parameters. The five alignment parameters and the two shape constants were fit using measurements at the three stage positions. In general, the χ^2 per degree of freedom for these fits was very satisfactory. The distributions of six of the fitted constants are given in fig. 26. The values for α_y include a common offset

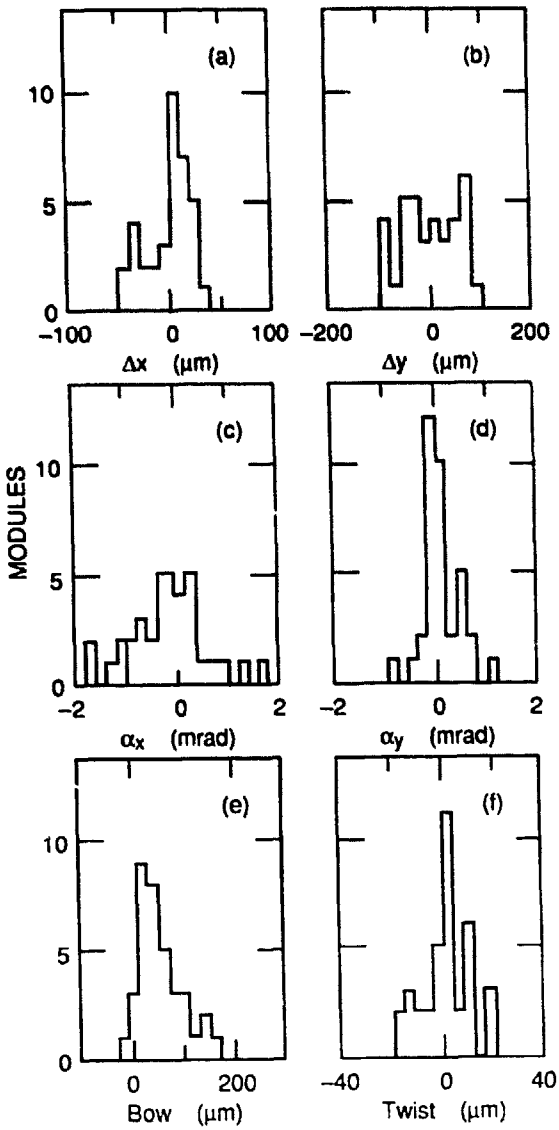

Fig. 26. Distributions of the alignment constants derived from the optical survey of the detectors. The effects of the bows and twists are given in terms of the maximum vertical offset relative to the center of an 80 mm long, 15 mm wide detector. Because of limited space, the distribution α_z is not shown here; it is the least critical of the fitted parameters.

of 0.05 and 0.17 mrad for all detectors in the two halves of the support structure. Such a common offset can be interpreted as a relative twist of the end pieces. The errors on the alignment parameters were $\sigma_x = 1$ μm, and $\sigma_y = 3$ μm, $\sigma(\alpha_x) = 0.05$ mrad, $\sigma(\alpha_y) = 0.02$ mrad, and $\sigma(\alpha_z) = 0.30$ mrad.

The contributions of the detector misalignment to the overall measurement error of the SSVD due to the 2 mm uncertainty in the extrapolated track position along the z axis was relatively small. For instance, $\alpha_x = 2.5$ mrad and $\alpha_y = 0.5$ mrad would each contribute an error of 1 μm. The effect of the bow term A can be translated to a maximum vertical displacement at the ends of the detector ($z = \pm 40$ mm) relative to the center at $z = 0$. A value of 50 μm would contribute less than 0.5 μm to the overall measurement error. Most of the detectors have much smaller bows. Similarly, the effect of the twist term B can be translated to a maximum displacement of the corners of the detector ($z = \pm 40$ mm, $x = \pm 7.5$ mm) relative to the center with $z = x = 0$. The effect of the twists was much smaller than that of most of the measured bows. Fig. 27 shows the worst example of a detector with bow and twist. The fit has rather large residuals and suggests the presence of a third order term. However, the maximum excursion of 20 ± 9 μm was not considered important.

7.3. X-ray alignment

The problem of determining the alignment parameters from the X-ray measurements was similar to the general one of computing the alignment degrees of freedom for any detector, given both the particle trajectories it measured and those measured in some external tracking system to which it was to be aligned. The external tracking system in this case was a set of precision stages that controlled the position and orientation of the SSVD, and the particle trajectories were those of the X-ray beam at the different stage settings. The formulation of a fitting procedure for the alignment parameters in this particular problem was discussed in detail elsewhere [30]; here a review of the method and results of the X-ray survey of the SSVD are given.

The setup for the X-ray alignment measurements is shown in fig. 28. One half of the support structure is mounted on a replica of the SLC vacuum pipe segment. The vacuum pipe was connected to a rotation stage which was mounted on an assembly of three

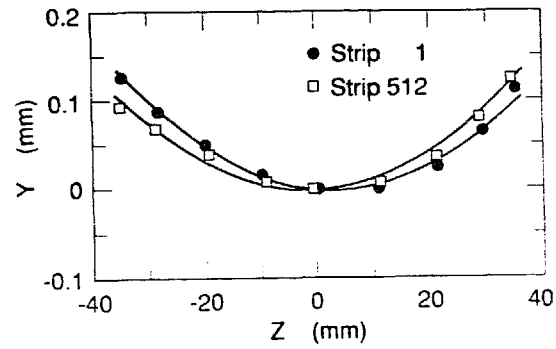

Fig. 27. Detector shape measurement for the detector with the worst bow and substantial twist. The two data sets represent the vertical (y) coordinates of the surface recorded along z for the first and last strips of the detector. The two lines give the fitted shape, $y = Az^2 + Bxz$ with $A = 94 \times 10^{-6}$/mm and $B = 65 \times 10^{-6}$/mm.

linear stages. Each stage was driven by a computer controlled stepping motor and could be positioned with an accuracy of 1–2 μm.

The rectangular structure in the center of the photograph housed the X-ray tube. The tube contained a water cooled tungsten target and was operated at a potential of 60 kV and a current of 25 mA. The X-ray beam was filtered by 0.8 mm of aluminum to attenuate the low energy end of the spectrum. The size of signal produced by the resulting beam in a silicon detector was fairly uniform as a function of the X-ray energy in the range of 15 keV to 50 keV. About 30% of the beam was absorbed in passing through a detector and its associated cable.

To collimate the X-ray beam, a pair of 3 mm thick tungsten slits was mounted on the bottom of a hollow brass cylinder that was attached to the X-ray tube housing. The collimator had a 50 μm × 2 mm opening which was oriented to be parallel to the detector strips. Given the length of the brass cylinder and the size of the X-ray source, a beam width of less than 100 μm in the x dimension was produced at all three module layers with the outer shell of the module housing placed a few mm below the collimator. The centroid of the X-ray beam was reconstructed to an accuracy of about 1 μm in x.

Before the alignment procedure began, a number of measurements were performed to verify that the stages were working properly. For example, the x stage linearity was checked by fitting the reconstructed beam position as a function of stage location. The rms of the residuals from these fits was generally 1–2 μm for a distance of travel of approximately 15 mm. Also, the slope determined from the fits was equal to unity to within one part in 10^4 which verified to this level both the scale of the stage and the spacing of the detector strips. In addition, measurements were also done to determine the trajectory of the beam in the reference frame of the stages.

Following the completion of these tests, alignment data were taken for one module at a time. Each detector was first centered below the collimator using the rotation stage. A sequence of scans of the type shown in fig. 29 was performed at five z locations. The settings of the stages together with the reconstructed beam positions were recorded. This process took about 20 min and was executed totally under computer control. It was then repeated until all 18 detectors in a given module housing had been measured.

The data obtained for each detector were used to fit the five alignment parameters and two shape parameters described earlier. The residuals from the fits, i.e. the deviations in x of the reconstructed beam positions from those predicted on the basis of the fitted parameters, had rms widths in the range of 2–4 μm. The repeatability of the alignment procedure was tested by measuring both halves of the SSVD two or three times. For each half, the measurements were made several

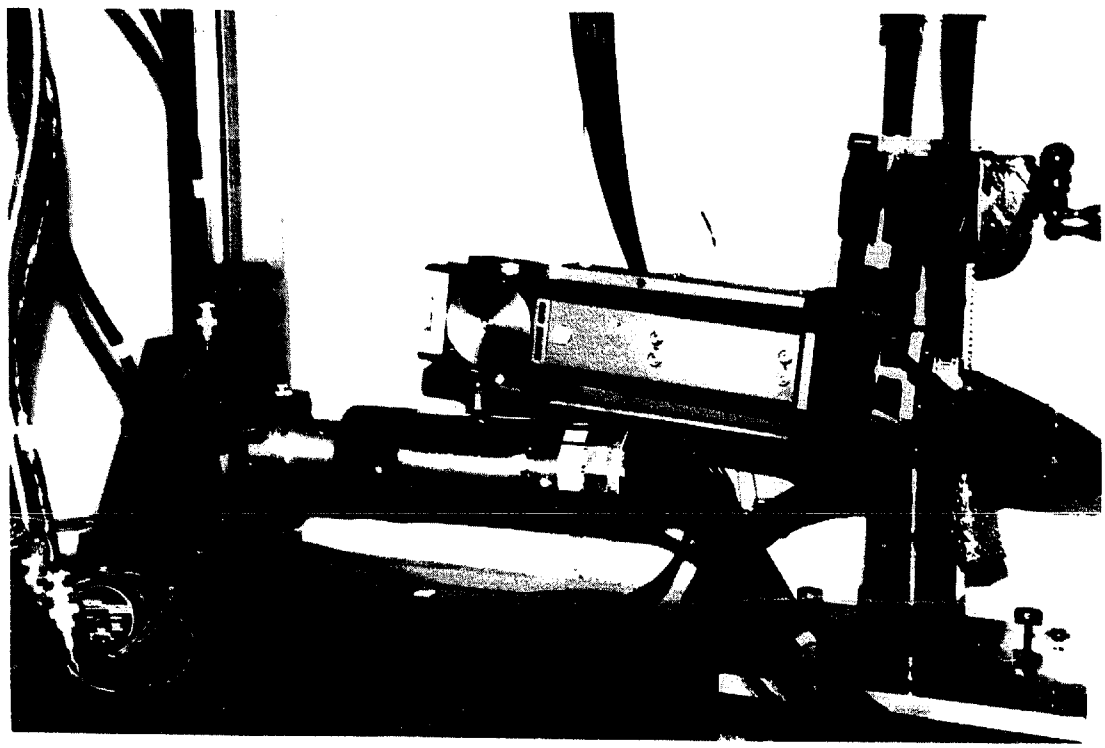

Fig. 28. Setup for the X-ray alignment, including precision translation and rotation stages, and the X-ray tube with the collimator. The detector modules installed in the SSVD support structure are prototypes for mechanical tests.

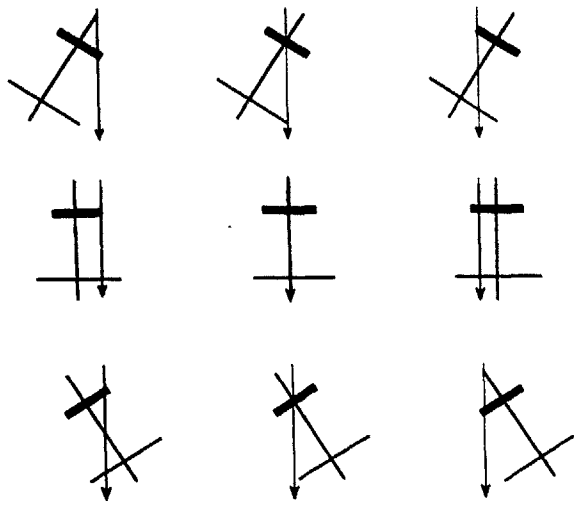

Fig. 29. Illustration of the positions and orientations of the detector (thick bar) relative to the X-ray beam (vertical arrow) during the alignment procedure. The axis of rotation is marked by the crossing of the two thin lines.

weeks apart with the housing detached from and then remounted on the vacuum pipe. To compare these measurements, it was necessary to fit for a global transformation to account for the small differences in the reference coordinate systems. A comparison of the x and y positions of the detector centers showed residuals that were generally consistent with the expected errors: 2 μm in x and 10 μm in y. However, for one half of the SSVD, it appeared that two of the detectors near one of its edges had moved by about 8 μm at the cable end of the detector. A probable explanation is that the cable clamp, which was weakest near this edge, allowed the flexible cables to move during the transfer to or from the vacuum pipe, and that the resulting force moved the modules.

Another effect that was observed during these tests was an apparent twist about the z axis of the each of the two halves of the SSVD. To match the x and y data at all z values, a term allowing for a common shift in α_y was required. The observed twists were equivalent to rotational offsets of 0.3 and 0.6 mrad of one end of the detector housing relative to the other. Such global shifts were not observed when the detector housing remained attached to the vacuum pipe between measurements. The observed twists might have been caused by an overconstrained mount of the detector housing or the cable clamp to the vacuum pipe.

7.4. Summary of detector alignment

In summary, the optical alignment procedure using fixed fiducials for transformations between reference frames produced very good measurement accuracy in three dimensions. Similarly, the X-ray survey resulted in accurate and reproducible data. A detailed comparison of the results showed systematic differences that were larger than the estimated measurement errors of either of the procedures. The cause for these differences is not understood. Potential problems could have arisen from the limited rigidity and limited precision of the light weight support structure. During the optical survey, the installation of the second and third layer could potentially have dislocated or bowed some of the detectors that had been inserted and measured before. Also, the outer thin shell and the rf shielding were not attached during the optical measurements and their installation could have exerted forces on the structure, possibly causing shifts or twists.

Many of the stability and rigidity problems could have been avoided with a support structure that was made of a single cylindrical piece and was mounted on the vacuum pipe prior to installation of the detectors. This solution was not practical for this experiment. Such a scheme would have also eliminated the need to detach the cable clamp and thereby risk pulling on individual modules during transfer of the loaded structure to another pipe.

7.5. The CDM system

To monitor changes in the position of the SSVD with respect to the surrounding vertex drift chamber, a system of capacitive sensors [33] was installed on the outside of the SSVD support structure. This system employed commercially-produced sensors and electronics [34] and was capable of measuring position changes to the level of a few μm. The capacitive displacement measurement (CDM) system detected changes in capacitance between sensors and electrically grounded pads. The system measured the voltage drop across a gap using a constant ac current source of a precisely controlled frequency and a low capacitance narrow band-pass amplifier tuned to this frequency. The ac voltage from the sensor was rectified and filtered to produce a dc output voltage in the range of 0–13 V. The dc voltages were digitized with an accuracy of 1 mV and recorded via CAMAC.

The design of the system is illustrated in fig. 30, which shows the placement of the sensors and ground pads. The sensors were recessed in the walls of the aluminium extensions to the outer shells of the SSVD support structure. The ground pads were epoxied to the beryllium inner wall of the VDC. The pattern of the copper pads was etched from a copper-coated kapton laminate of 0.5 mm thickness. To measure the six degrees of freedom that define the placement of each half of the SSVD relative to the VDC, seven sensors (plus three spares) were installed on each half shell, two each for x and y, one for z, and to enhance the sensitivity, two for α_z, the rotation around the

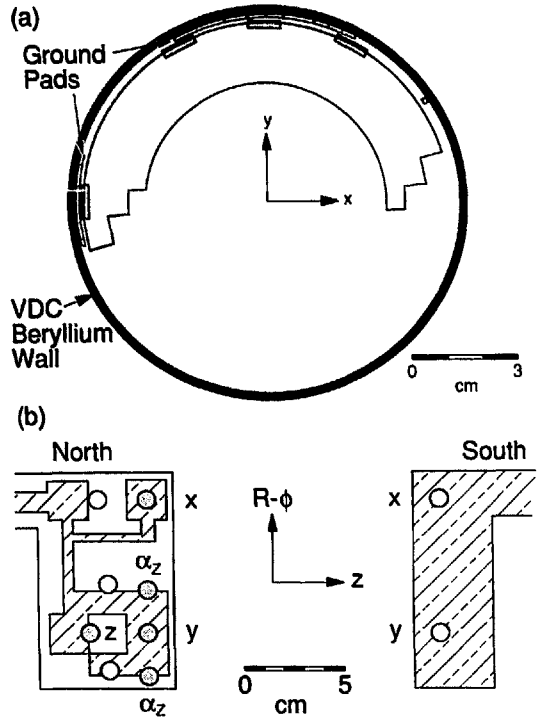

Fig. 30. Placement of the CDM sensors (shaded circular spots) and copper pads (hatched regions) (a) in the $x-y$ projection, viewed from the direction of the positron beam (south) and (b) in an $r\phi-z$ projection, viewed from the beam–beam interaction point. The sensors labeled x (y) measured translations parallel to the horizontal (vertical) axis and by comparison of the readings at the two ends, rotations about the vertical (horizontal) axis. The z sensor measured translations parallel to the longitudinal axis, while the two sensors marked α_z detect rotations about the longitudinal axis. The locations of the spare sensors are marked by open circles.

z axis. Three spares were added to backup the z and α_z sensors, in case a large misalignment of the pads and sensors occurred during installation.

Translations along the x and y axes and rotations about those axes were derived from measurements of changes in the gaps between the sensors and ground pads. Thus the x and y sensors fully overlapped the pads. A typical calibration curve for a gap measurement is shown in fig. 31a. For gaps of up to 1 mm the response was linear with a slope of 3.70 V/mm, for larger gaps the response decreased monotonically. The sensors had to be precisely calibrated to retain a precision of better than 1 μm.

To sense displacements parallel to and rotations about the z axis, motions of the sensors parallel to the pads had to be measured. In this case, the change in capacitance was caused by a change in the overlap of the sensor and the ground pad, and was greatest when the edge of the ground pad was approximately centered on the sensor. Fig. 31b shows the variation in voltage as a function of the parallel displacement of the sensor relative to the edge of the ground pad for an insulator thickness of 0.5 mm and a gap of 1.35 mm. The slope of 0.167 V/mm indicates that a 1 mV error in the voltage measurement would result in a position error of 6 μm. Since the measured sensor voltage is a function of both the gap size and the pad overlap, and the sensitivity to overlap changes is only 1/20 of that of gap changes, measurements derived from these probes have much larger systematic errors than the measurements of motion perpendicular to the gap.

Prior to installation, the entire system was calibrated in a setup that simulated the geometry of the cylindrical walls of the silicon detector and vertex drift chamber, allowing accurately-measurable motions (to 2 μm precision) in all six degrees of freedom. During the operation in the Mark II detector, two additional sensors with a fixed gap of 1 mm with respect to a ground pad were used to monitor the stability of the electronic

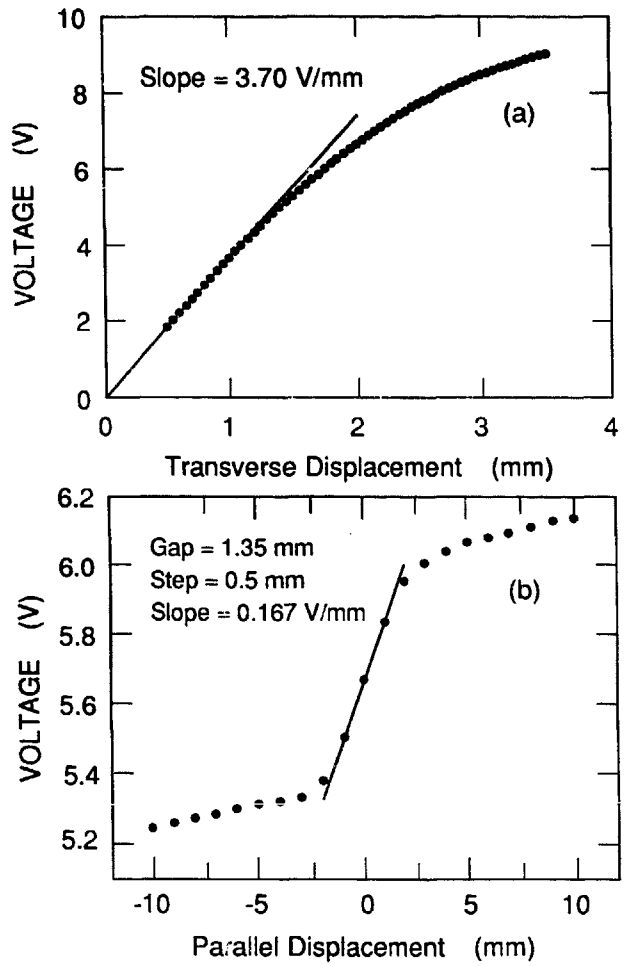

Fig. 31. Calibration of the CDM sensors: Output voltage versus displacement for (a) transverse motion and (b) parallel motion of the sensor relative to the edge of the ground pad (for a Kapton insulator thickness of 0.5 mm and a gap of 1.35 mm).

readout. To avoid random pickup on the 15 kHz clock signals, the sensors at the two ends of the SSVD were pulsed separately rather than driven by a common clock.

A sample of measurements illustrating the performance of the CDM system over a period of four days is shown in fig. 32. Several features are apparent from these data which were recorded after installation of the SSVD in the Mark II detector. Substantial changes in positions and angles occurred when the large Mark II solenoidal magnet was turned on or off. This is not surprising since some of the vacuum pipe supports were attached to the steel endcaps that had been observed to move by as much as 1 mm when the magnet was powered up. Another feature of the data are the diurnal variations which were largest in the vertical direction (on the order of 20 μm). There are two contributions to these variations, one from actual motion of the detector, the other from shifts in the CDM voltages due to temperature variations. The fixed sensor measurements indicated that temperature variations caused common voltage shifts at the level of a few mV which corresponds to a change of about 0.5 μm (12 μm) in the transverse (longitudinal) position. This is consistent with a comparison of data from the lower and upper half of the SSVD which show rms differences in the vertical and horizontal displacements at this level. This observation places a limit not only on the real differences in motion, but also on systematic effects on the CDM amplifiers due to temperature variations. The angular motion about the transverse axes was derived from differences in the readings of sensors separated by 15 cm, thus a rotation of 10 μrad corresponded to a relative gap change of 1.5 μm. The angular motion shown in fig. 32 is less than 10 μrad over the monitored period of 80 h following the magnet turn on. For the z and z measurements, the rms spread of the data in fig. 32 is comparable to the estimated systematic errors of 10 μm and 100 μrad. A rotation of 100 μrad corresponds to a 4 μm azimuthal displacement of the sensors relative to the edge of a ground pad.

In summary, based on the CDM system there is evidence for a diurnal transverse motion of the vacuum pipe of approximately 20 μm, and no evidence for significant rotations or longitudinal motion, except for instabilities caused by the turn on of the Mark II magnet. Over the course of several months slow drifts on the order of 20 μm were observed. Systematic errors in the measurement of transverse displacements were estimated to be 0.5 μm over periods of several days and less than 3 μm over several months.

Since relative changes in position were the principal concern, the detector motions were referenced to an initial reading. Due to removal of the detector endcaps during the course of the run, the reference readings had to be reestablished several times.

8. Operation in the Mark II at SLC

The SSVD detector was installed on the vacuum pipe and inserted into the Mark II detector in December 1989. Following a two week engineering run in

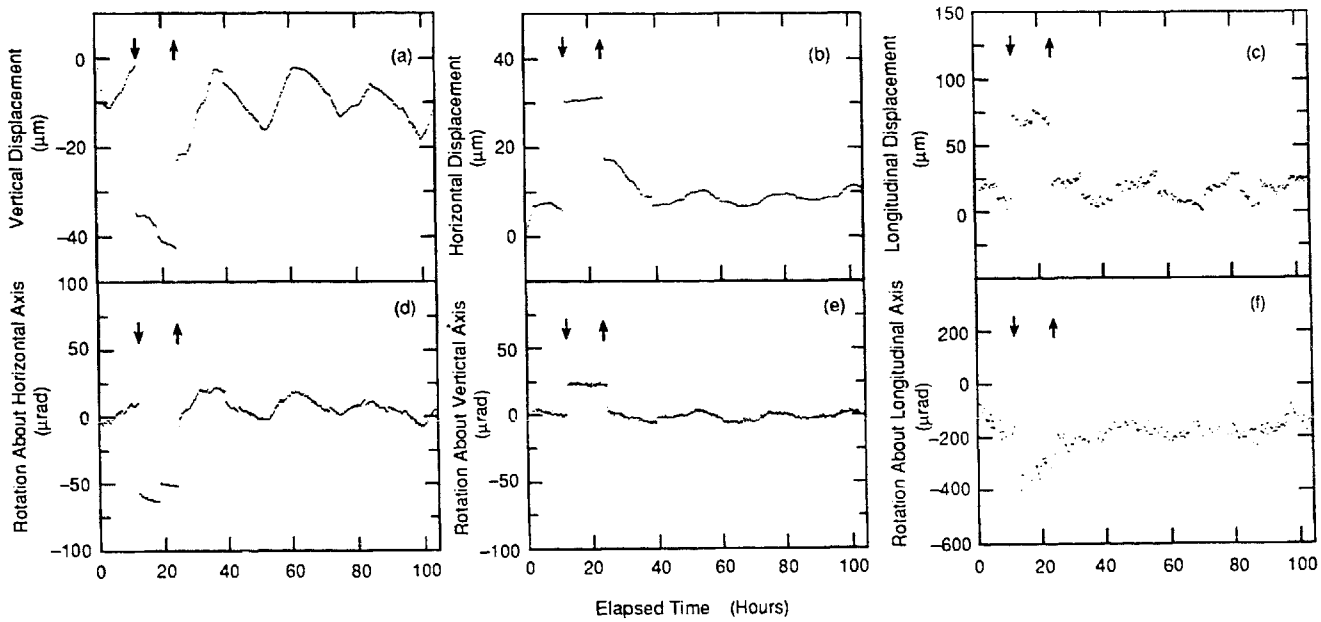

Fig. 32. Motion of the upper half of the SSVD relative to the VDC recorded during a run of 106 h duration: (a) vertical, and (b) horizontal and (c) longitudinal displacement, and rotations about the (d) horizontal (e) vertical, and (f) longitudinal axis. The arrows indicate the times when the Mark II solenoidal magnet was turned off (↓) and on (↑).

January 1990, data were recorded intermittently during the months of July to November of the same year. Since machine studies were given priority during this run, the colliding beam operation was frequently interrupted. The total integrated luminosity was 10.1 ± 0.7 nb^{-1}, yielding 269 hadronic and 25 leptonic decays of the Z^0. The data set was partitioned into three samples, each sample starting with a major disturbance of the vacuum pipe and thus requiring a redetermination of the location of the SSVD relative to the outer tracking systems. The samples, denoted as I, II, and III, contained 37, 84, and 173 Z^0 decays, respectively.

8.1. Beam background and radiation dose

During operation at the SLC, beam background rates varied strongly depending on the steering and focussing of the beams. The machine parameters were adjusted so as not to severely affect the operation of the Mark II detector elements. The occupancy in the SSVD, defined as the fraction of channels with a pulse height greater than $1.5\sigma_i$ was on average 2.5% for events containing a hadronic Z^0 decay. For randomly triggered events with and without beams colliding at the interaction point, the average occupancy for the SSVD was 1.7% and 0.005%, respectively. During machine studies and periods of machine tuning much higher instantaneous background rates were experienced.

Several thermoluminescent dosimeters were attached to the SSVD housing on both sides of the interaction region during the operation of the detector. The measured absorbed doses depended on the location of the monitors; they varied between a minimum reading of 62 rad and a maximum of 127 rad on the detector ends facing the incoming electron and positron beams, respectively. These levels of radiation were substantially lower than expected during the commissioning of the SLC. They were also well below the levels at which noticeable changes in the operation of the Microplex chip were expected.

8.2. Voltage and current monitoring

The detector bias voltages and leakage currents, as well as various supply voltages for the Microplex circuit that were critical for the performance of the SSVD, were monitored continuously. A description of the monitor system is given in section 5.4.

With the exception of one module, the leakage currents increased by less than 1 μA over a period of five months. During the same period, the average single-channel noise for all modules increased by about 5%. The maximum variation of the single-channel noise throughout the data taking was about 25%. The average pulse height per charged track was stable to better than 5%, indicating that the gains per channel remained essentially constant.

8.3. Pedestal stability

Pedestals were measured and recorded approximately every eight hours, and were updated event-by-event by the BADC. During a typical two-hour run, the rms of the pedestal shifts of individual channels was less than one-half of the single-channel rms noise. Over the total data taking period of five months, the average of the maximum pedestal change per channel was comparable to the pulse height resulting from a minimum-ionizing particle. This observed pedestal stability indicated that the various control signals and supply voltages upon which the pedestals depended were very stable.

On a few occasions, the pedestals of all strips on one or two modules underwent sudden shifts by 400 or more BADC units corresponding to three times the average signal for a minimum ionizing particle. The pedestals of all channels of an affected module changed by approximately the same amount, except for one case, when alternate channels experienced pedestal shifts of opposite polarity. On nine occasions, the pedestals decreased from their nominal values, and on three occasions, the pedestals of these modules shifted back to the their original values after they had remained low for as long as several months. The pedestals of three other modules returned to their original values within a few hours after the initial shift. No increase in the detector leakage currents was observed in conjunction with the pedestal shifts, and the operation of all but two modules remained unaffected. For these two modules, the noise, gain, and signal-to-noise ratio decreased substantially after the drop in pedestals, such that for roughly 10% of the strips, the signal-to-noise ratio fell below 10. One of these two modules experienced a second pedestal shift two months after the first and its pedestals, noise, gain, and signal-to-noise ratio all returned to their original values.

A total of twelve incidents affecting six different modules were observed. Nine of them occurred immediately after significant beam losses were recorded near the interaction point. One occurred after several days of machine operation with unusually high radiation levels. For the remaining two incidents, no record of the radiation levels near the detector was available. The radiation exposure of the SSVD preceding these shifts is not precisely known, but was most likely only a few rad. Of the six affected detector modules, four were located in the first and two in the second layer, and all but one near the horizontal plane, i.e. at locations were the radiation dose was largest.

There were many incidents of comparable exposure to beam background, instantaneous and extended,

Table 2
Summary of the detector channels that were not read out because of failure to meet the performance criteria. The numbers are to be compared to a total of 18432 channels for 36 detector modules

Item	Problem	Number of channels N_{ch}	Fraction of data lost f	$N_{ch} f$
1	thin cable damage	511	1.00	511
2	external cable damage	511	0.62	315
3	guard ring wiring	36	1.00	36
4	detector edges	296	1.00	296
5	pedestal shifts	1533	0.03	49
6	low signal/noise	214	1.00	214
7	diode failure	64	0.88	56
	sum items 3–7	2145	0.30	647

without any noticeable pedestal shifts. The mechanism responsible for the observed pedestal shifts is not understood.

8.4. Failing detector strips and readout channels

During the course of the data taking, the performance of the readout channels was monitored regularly. The channels that failed to meet the performance criteria were labeled as bad in the BADC database and excluded from readout. Table 2 lists the various failure modes, the number of channels affected, the fraction of time during which the channels failed, and the average number of channels failing during the course of the run. A few words of explanation are warranted here:

1) On one of the detector modules, the trace on the thin cable that carried the detector voltage broke during installation. As a result, this detector could not be operated.

2) One of the external cables was cut during the removal of the Mark II endcaps and developed an electrical short circuit that rendered the module unusable for the rest of the data run.

3) The bonding pad for channel 512 on all modules was purposely connected to the guard ring rather than an amplifier, thus the number of strips per detector connected to the readout was 511.

4) Typically the five strips closest to each of the detector edges exhibited large leakage currents and poor signal/noise ratios and were labeled as bad. The increased noise was attributed to charge collection near the guard ring. As a consequence, the effective active width of the detectors was reduced by 0.25 mm to 91–92% of the total detector width.

5) The sudden large pedestal shifts described above resulted in a loss of data for a few hours at a time, until the pedestal change was recorded in the BADC database.

6) In addition, 214 isolated channels were found to have poor signal/noise performance. Most of these channels were identified in the course of the gain calibrations performed with the ^{241}Am source prior to installation. About 20% of the failures occurred in exactly the same location on the detectors for layer III, and thus were attributed to a mask defect in the detector fabrication.

7) Three of the 35 operating modules developed one or two regions of eight or more adjacent strips with very large negative pedestals. No measurable increase in the detector leakage current was found in connection with these failures. The cause of the problem is not known, but the observed features resembled those caused by a decrease in the interstrip resistance due to the accumulation of electrostatic charge on the detector surface. Three of the four defects developed during the first operation of the detectors at the SLC; one was already present during the initial module tests.

In summary, two of the 36 detector modules had damaged data cables that caused complete failure. Of the remaining 34 modules with 17408 readout channels, on average 647 were not operational. Only 1.6% of all channels failed because of detector defects or malfunctioning electronic circuits.

9. Track reconstruction in the SSVD

Charged particle track reconstruction began in the two wire chambers surrounding the silicon strip vertex detector. The central drift chamber (CDC), which had been in operation at SLC prior to the installation of the vertex detectors, had 72 layers of signal wires and extended from 19.2 to 151.9 cm in radius [5]. The position resolution per wire averaged over the drift cell was measured to be 170 μm. The CDC was well tested and programs for pattern recognition and track fitting were well understood [35]. The vertex drift chamber (VDC) consisted of 10 jet cells with 32 active signal wires at radii between 5.1 and 16.6 cm. The jet cells were tilted by about 15° relative to the radial line to facilitate the resolution of the ambiguity in the drift direction, to provide a large sample of tracks crossing the cathode plane for calibration purposes, and to avoid losses due to tracks close and parallel to a wire plane. The chamber was operated with a 92%–8% mixture of CO_2–ethane at 2 bar [6,7]. On the basis of high energy cosmic rays, the position resolution of tracks extrapolated to the center of the detector was measured to be 35 μm and the angular resolution was 0.5 mrad. These values are roughly 30% worse than

expected. To assure a reliable measurement of the track parameters, all tracks were required to have at least 25 of 72 possible hits in the CDC, and at least 15 of 32 possible measurements in the VDC.

Fig. 33 shows a two-jet decay of the Z^0 as recorded in the vertex detectors. The raw signals, including signals generated by beam background, are displayed. The high momentum charged particle tracks originating from the beam–beam interaction point are clearly recognizable both in the VDC and the SSVD. Though the azimuthal gaps between the silicon detectors lead to geometric losses, the high efficiency of the detectors is apparent. Only a small fraction of the pulse height clusters in the SSVD are not associated with tracks reconstructed in the outer chambers.

To check for errors in the tracking algorithms, and to obtain a better understanding of the performance of the vertex detectors a Monte Carlo simulation of the data was performed. This simulation included not only the production and hadronic decays of the Z^0, and subsequent particle decay and multiple scattering [36] in the beam pipe material and the detectors, but also detector geometry with alignment error for individual modules. Other parameters, such as the position resolution and detection efficiency, taking into account losses due to malfunction of individual strips, were derived from the data and included in the simulation. Effects of beam-related background hits were simulated by overlaying Monte Carlo generated events with events recorded with random triggers. Also, the effect of the transverse motion of the beam–beam interaction point was taken into account by introducing a Gaussian beam profile with a width corresponding to the experimentally observed value. On the basis of simulated event samples, the impact of different effects on the track reconstruction could be studied.

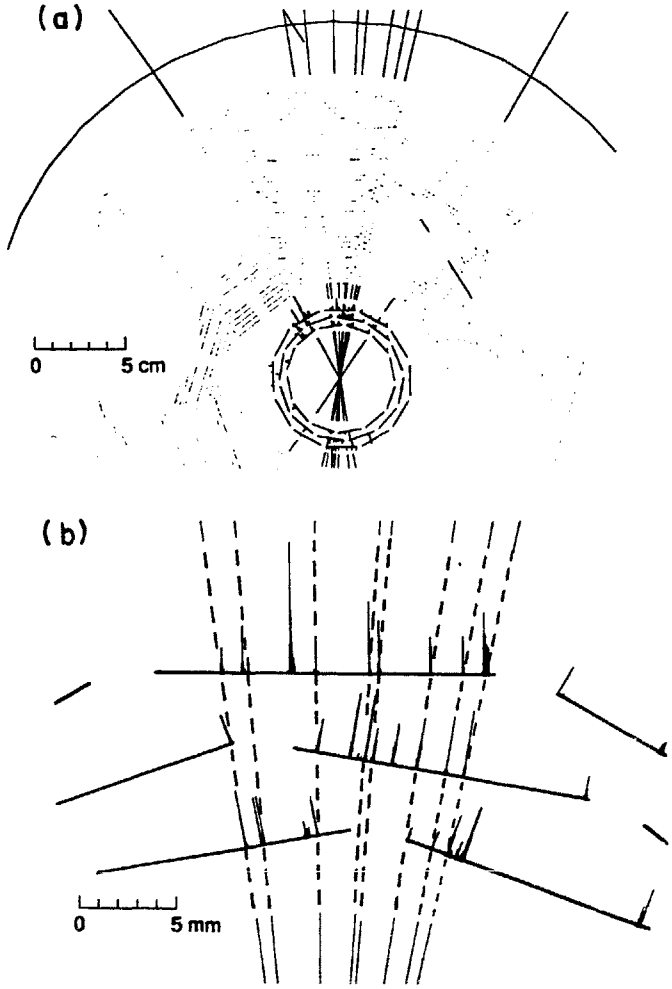

Fig. 33. Display of a reconstructed Z^0 decay in the Mark II vertex detectors, with the SSVD in the center and the VDC surrounding it, showing the digitizations in (a) the SSVD and one half of the VDC, and (b) a small section of the SSVD. Charged tracks that have been reconstructed in the CDC are marked as straight lines originating from the beam–beam interaction point. Due to the ambiguity in the direction of the drifting charge, all hits in the VDC, marked as dots, are plotted twice. A large fraction of the hits were generated by beam background. For the SSVD, the recorded pulse heights per strip are indicated in the form of small histograms on the detectors.

In the following, the procedures for track finding and track fitting in the combined tracking system are discussed. This involves the association of the signals detected in the SSVD with tracks extrapolated from the outer chambers, the global survey of the SSVD relative to the other tracking devices, and the internal alignment of the individual modules of the SSVD.

9.1. Cluster finding

A charged particle traversing a silicon strip detector ionized the silicon along its path. The point of impact of the particle, measured at the detector mid-plane, was determined from the centroid of the collected charge distribution, defined as the pulse height weighted average strip position. Operationally, a cluster was defined as a group of contiguous detector strips with a pedestal corrected pulse height per strip of more than $1.5\sigma_i$ where σ_i is the rms noise of the individual strips. In addition, at least one strip per cluster was required to have a pulse height greater than $5\sigma_i$. Clusters adjacent to, or containing known bad strips, were excluded from the analysis.

To identify clusters that were generated by two very closely spaced tracks, all clusters were examined for dips in their pulse height profile. If a pulse height dip with a significance of more than $1.5\sigma_i$ was observed, the cluster was divided into two, provided each half included at least one strip with a pulse height greater than $5\sigma_i$. The pulse height of the central strip between the two halves was shared equally between the resulting pair of clusters. This algorithm was expected to work well for track separations of two or more strips. The algorithm resulted in offsets of both half-clusters by a few μm, and the offsets increased with smaller track separation. On average, roughly 1% of all tracks were affected by merged clusters.

On average, the number of pulse height clusters detected per Z^0 event was 2.8 per detector module. For random events with and without beam, there were 1.7 and 0.003 clusters per module, respectively. The latter value is of the order of magnitude expected for clusters generated by the detector noise given the $5\sigma_i$ threshold cut. While there was on average about one Z^0 associated track per module, jet-like Z^0 events caused a much higher density of tracks locally.

Distributions of the number of strips and pulse heights per cluster are given in fig. 34, separately for clusters that are, and that are not, associated with charged particle tracks. Track-associated clusters tend to be narrower and have less of a variation in pulse height than background clusters. Most of the background clusters were generated by photons and charged particles that originated from photons created by interactions in one of the beam masks or the vacuum pipe.

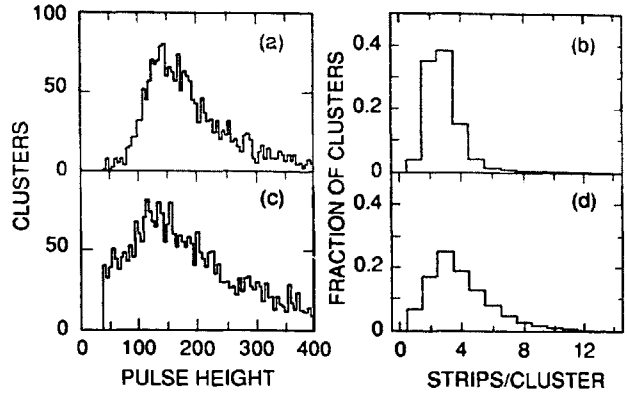

Fig. 34. Distribution of cluster pulse heights and the number of strips per cluster for clusters that are ((a), (b)), and are not ((c), (d)), associated with a track.

These dominantly low energy particles traversed the detectors at large angles, leading to large energy depositions in the SSVD. While there are marked differences between the distributions for background and track generated clusters, the differences are not large enough to permit a clear distinction on a cluster by cluster basis.

A measurement of the signal-to-noise ratio for minimum ionizing particles was derived from the observed pulse height distribution for track associated clusters. This ratio was defined earlier as the total cluster pulse height divided by the rms noise of a single channel. Here, the average of the noise of all strips forming the cluster was used. Fig. 35 shows the signal-to-noise ratio distribution for clusters associated with tracks of more than 0.5 GeV/c transverse momentum. The data were averaged over all detector modules. The cluster pulse heights were corrected for non-relativistic momenta and non-normal incidence. All tracks were assumed to have pion mass, even though roughly 10% of the tracks in this sample were expected to be kaons or protons. The most probable ratio is comparable to the value of

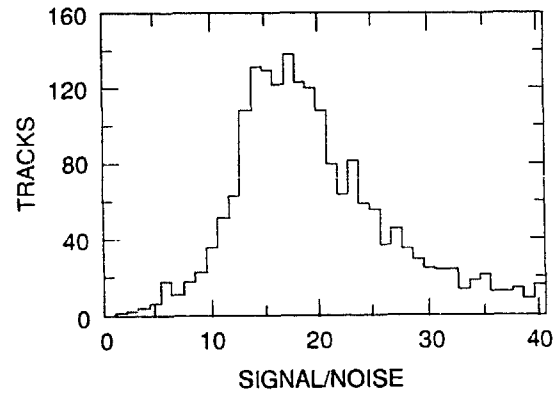

Fig. 35. Measurement of the signal-to-noise ratio for charged tracks, corrected for non-normal incidence and non-relativistic effects.

17.6 expected on the basis of the measurements performed with the ^{241}Am source prior to installation.

9.2. Track finding

The initial estimate of the five parameters ($1/p_{xy}$, ϕ, tan λ, b_{xy}, b_z) that define a track was obtained from a fit to the CDC and VDC data. Here p_{xy} is the component of the track momentum transverse to the beam and the direction of the magnetic field, ϕ is the azimuth angle, λ is the dip angle relative to the x–y plane, b_{xy} is the distance of closest approach to the origin in the transverse plane, and b_z is the z coordinate of the track at the point of closest approach in the x–y plane.

For the purpose of associating hits in the SSVD with the tracks reconstructed in the CDC and VDC a least-squares fit was performed [37,38]. In addition to the five track parameters measured in the outer wire chambers, the transverse distances of closest approach of the projected tracks to the SSVD hits were input to this fit. For three SSVD hits, a 8×8 covariance matrix was formed from the 5×5 covariance matrix provided by the track fit and the 3×3 error matrix for the SSVD hits. Multiple scattering errors were added for each layer of material in the tracking volume which affected the measured hit positions. A list of the material contributing to the multiple scattering, including the vacuum pipe, the SSVD and the VDC is given in table 3. The multiple scattering introduced correlations between measurements in the individual layers of the SSVD and the track parameters. The fit resulted in an improved set of track parameters and corresponding covariance matrix. Since the SSVD did not measure z coordinates, the new fit had little effect on λ and b_z. Also, the momentum measurement was not improved significantly.

Operationally, the tracks were extrapolated into the SSVD volume and all possible combinations of clusters within a distance of about 1 mm from the extrapolated track were taken as candidates for associated signals. The selection of clusters was done sequentially, trying to maximize the number of SSVD hits associated with a track. Sets of three, two, and one clusters were tried, and the set with the largest number of clusters and the best match to the track, i.e., the lowest χ^2/dof, was selected, provided it fulfilled the condition $\chi^2/\text{dof} < 5$. Here dof refers to the number of degrees of freedom, and equals the number of clusters per set. Clusters were not allowed to be associated with more than one track. In case of an ambiguity, the track with the higher momentum was selected.

The selection procedure was designed to assure the correct association of the SSVD hits with the external tracks while maintaining a high track finding efficiency. A cut of $\chi^2/\text{dof} > 5$ was expected to reject 2.5% of single hit, 0.7% of two-hit and 0.2% of three-hit fits, provided the correct measurement errors were used. Clusters affected by background hits and tracks poorly measured in the outer wire chambers lead to additional losses. A Monte Carlo simulation taking into account beam generated background, bad strips in the SSVD, the alignment procedure for the SSVD, and realistic tracking errors in the VDC agreed reasonably well with the measured multiplicity of hits in the SSVD as shown in table 4. Not included in the table are the approximately 6% of all tracks found in the outer chambers which ended up without any SSVD hits.

To determine the efficiency for detecting a charged particle traversing a single silicon detector, all combi-

Table 3
Thickness of material (in mm and units of radiation length X_0) in the vertex tracking system, including the vacuum pipe with the wire profile monitor and beryllium walls of the SSVD and VDC. The frames for the wire monitors are mounted inside the vacuum pipe and cover roughly 11% of the azimuthal acceptance

Item	Material	Radius [mm]	Thickness [mm]	Thickness X/X_0 [%]
Wire monitor frame	Al	23.7	0.8	0.90
Beam pipe	Cu	25.0	0.025	0.17
	Al		0.483	0.54
SSVD inner shell	Be	27.6	0.38	0.11
SSVD modules layer I	Si	29.4	0.315	0.335
	Cu		0.012	0.084
	kapton		0.15	0.052
	epoxy		0.075	0.025
SSVD modules layer II	total	33.7		0.50
SSVD modules layer III	total	38.0		0.50
SSVD outer shell	Be	41.0	0.38	0.11
VDC inner wall	total	44.0	1.76	0.85
VDC active region	Cu		0.08	0.60
	Gas		130	0.12
VDC outer wall	total	180		5.32

Table 4
A comparison between the data and the Monte Carlo simulation for the number of clusters in the SSVD associated with charged particle tracks of more than 150 MeV/c transverse momentum. The numbers represent the fraction of all tracks with at least one associated hit in the SSVD

Number of hits	Fraction of tracks [%]	
	Data	Monte Carlo
1	17 ± 2	15
2	57 ± 2	59
3	26 ± 2	26

nations of cluster pairs for tracks with two or more clusters were considered. For the straight line defined by a pair of hits, the position of impact on a detector in the other layer was calculated. To avoid known inefficiencies, this detector had to be free of any known bad readout channels within at least 10 strips of the projected track impact. In addition, to avoid confusion and effects of background hits, all tracks in the sample were required to be separated from any other track by at least 15 mrad in azimuthal angle, and each cluster had to be separated from any other cluster by at least 30 strips. A sample of 731 pairs of clusters satisfying these conditions was found. Of these pairs, 730 had a cluster located within 3 strips from the projected position. Thus with these criteria, the efficiency for detecting a charged particle was $99.9 \pm 0.1\%$. At the position of the missing cluster, a strip with a pulse height of $4\sigma_i$ above pedestal was found, just failing the $5\sigma_i$ pulse height cut.

9.3. Alignment based on tracks

The individual silicon detector modules in each of the two halves of the SSVD were surveyed optically and with a collimated X-ray beam prior to installation in the Mark II (see section 7). It was hoped that the only task remaining after the installation would be the global alignment of each half with respect to the overall coordinate system of the Mark II. However, as soon as tracks were available it became apparent that a global alignment alone would not be sufficient to locate the individual modules to the needed accuracy. Consequently, charged particle tracks had to be used not only to determine the global alignment, but also to check and correct the alignment constants for individual detectors. In addition, any motion of the SSVD relative to the surrounding VDC was monitored by the CDM system (see section 7.5) during the data taking. The observed changes were taken into account, though they were small compared to the sensitivity of the track fits to global changes in alignment.

The position of each of the two halves of the support structure can be described in terms of three positions and three angles. They are defined in the Mark II coordinate system, with z pointing in the direction of the electron beam, x horizontal and y vertical. The global offset in z did not need to be precisely known and it was derived from the measured tracking efficiency rather than a fitting procedure. As described earlier and illustrated in fig. 25, seven parameters define the orientation and position of each detector relative to its nominal position in the support structure: three angles, α_x, α_y, and α_z, and two linear offsets, Δx and Δy, plus two shape parameters accounting for a bow and a twist. Since the strips run parallel to the z axis, no local offsets Δz are needed.

The global and local alignment constants were determined by a least-squares fitting procedure that minimized the distances and angles between the tracks reconstructed in the wire chambers and the track segments in the SSVD. Since the hits in the SSVD had to be selected by projecting tracks reconstructed in the outer wire chambers into the SSVD, the alignment and hit selection were iterative procedures. However, the process converged quickly due to the excellent resolution and granularity of the silicon strip detectors and the position and angular precision of the VDC. Approximately 2100 tracks with transverse momenta greater than 0.5 GeV/c and with hits in at least two of the three SSVD layers were used in the alignment fits. Roughly a third of the selected tracks had hits in all three layers of the SSVD.

To formulate the alignment procedure, the following variables were introduced [38]: for-tracks with hits in layers j and k,

$$\Delta b_{jk} \equiv (\xi_j + \xi_k)/2,$$

$$\Delta \phi_{jk} \equiv (\xi_j - \xi_k)/\Delta r_{jk},$$

and for tracks with hits in all three layers,

$$\Delta b_{123} \equiv (\xi_1 + \xi_2 + \xi_3)/3,$$

$$\Delta \phi_{123} \equiv (\xi_1 - \xi_3)/\Delta r_{13},$$

$$\Delta \delta \equiv (\xi_1 - 2\xi_2 + \xi_3)/2.$$

The variables ξ_j are the miss distances between the extrapolated position of the track measured in the wire chambers and the measured hit in layer j of the SSVD. The radial distances between different layers of the SSVD are denoted by Δr_{jk}. The variables Δb_{jk} and $\Delta \phi_{jk}$ are most sensitive to the transverse position and angle of the track, while the variable $\Delta \delta$ measures the intermodule alignment and is relatively insensitive to the global alignment constants.

The alignment constants were determined by fits that minimized the sum of the squares of the relevant Δ variables, divided by their measured variances. The sum included all tracks with two or more hits in the SSVD. Correlations between the Δb_{jk} and $\Delta \phi_{jk}$ variables for a given track were not included in the χ^2, since their effects, averaged over all tracks, tended to be small. Fits were performed separately for the global and local alignment constants, and 2–3 iterations were necessary to determine a consistent set of constants, indicated by values of χ^2/dof close to unity. The five global constants per detector half were fit separately for each of the three running periods; only one set of local constants was used for the entire data sample.

For the local alignment, the three most significant parameters were the transverse and radial offsets, Δx and Δy, and the yaw angle, α_y. The sensitivity to the roll and pitch angles, α_z and α_x, and the shape param-

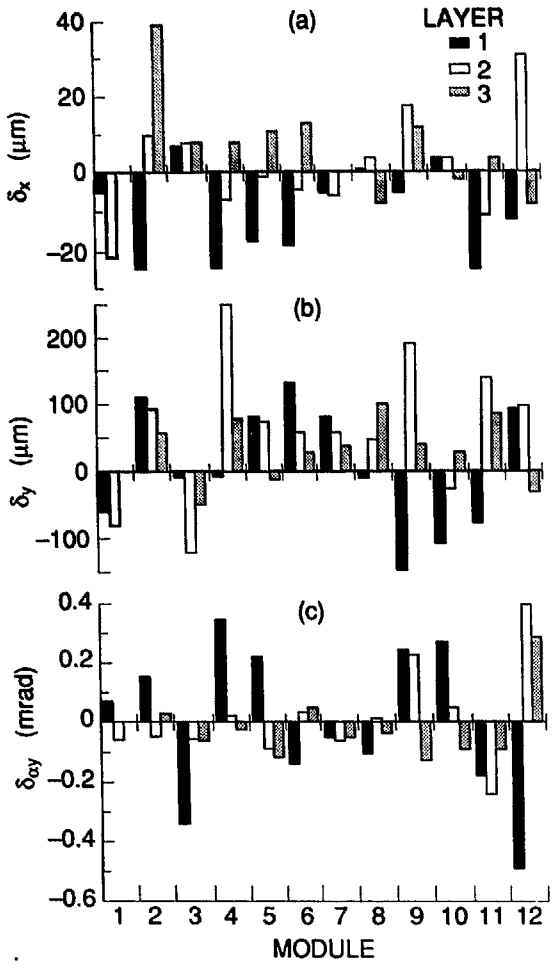

Fig. 36. Results of the alignment of the individual SSVD modules using tracks: The distributions show the changes in the constants relative to those obtained from the X-ray survey, (a) the transverse offset δx, (b) the radial offset δy, and (c) the angular offset $\delta\alpha_y$.

eters bow and twist was marginal and reflected the fact that the track measurements were not very sensitive to the small displacements described by these variables. Thus, they were not included as free parameters in the alignment fit, except as a cross check to assure that the values obtained from the X-ray measurements were adequate. In total, 105 alignment constants for 35 modules were determined from a fit to the selected tracks. Corrections for global motions as monitored by the CDM system were applied but had little effect on the results.

The results of the realignment of the individual detectors are given in fig. 36 in terms of the change in the alignment parameters relative to the X-ray survey performed about a year earlier. In the comparison of the two sets of alignment constants, global rotations and translations have been removed. Also removed were shifts in α_y common to the detectors in each half of the support structure, namely −0.76 mrad for the top, and −0.36 mrad for the bottom. These shifts represent twists of the half cylinders, similar to those observed during the X-ray alignment (see section 7.3). Uncertainties in the fits are estimated to be typically 5 μm for the transverse offsets, 25 μm for the radial offsets, and 0.1 mrad for the yaw angle. The rms of the changes is 13 μm in the transverse and 78 μm in the radial direction. The rms of the angular changes is 0.12 mrad. The corresponding maximum changes are 40 μm, 250 μm, and 0.5 mrad. The sensitivity of the alignment fit to statistical fluctuations and systematic errors was studied in detail by subdividing the data sample into various subsamples. No significant effects were found.

It is obvious from the data in fig. 36 that for many modules the measured offsets in one or more parameters exceed the fit errors by substantial factors. There is no discernable pattern in the data and nothing points to a simple explanation for the cause of these changes, although systematic errors in the X-ray survey cannot be ruled out with complete certainty. As was pointed out earlier, there is evidence from the optical and X-ray alignment data that individual modules did not maintain their position to the desired level of a few μm. Thus they may have moved, perhaps during the testing that occurred prior to installation, during the installation on the vacuum pipe, during a series of earthquakes, or during subsequent temperature changes. However, there is no evidence for any significant instability over the period during which the data were recorded.

Given that each silicon module overlaps in azimuth with two modules in each of the other two layers, one would naively expect that the alignment procedure strictly constrained the relative positions of modules in different layers. This would indeed be the case, if the track angles (measured relative to the normal on the detector plane) were large or if the transverse offsets, Δx, were the only alignment parameters that were free to vary in the fit. As illustrated in fig. 37, the position of module A is coupled to that of module B which in turn is coupled to module C, etc. If one also allows the radial offsets, Δy, to vary the situation changes significantly. The parameters for module C are now coupled to a linear combination of the transverse and radial offsets of module B. As a result, the placement of module C becomes largely decoupled from module A. For tracks of nearly perpendicular incidence, module B can move radially without affecting the position of hits on the tracks passing through module A. For modules in different layers that overlap in azimuth, the correlation coefficients for the offsets Δx have typical values of 0.6, whereas for adjacent modules in the same layer the correlations are surprisingly weak, less than 0.1.

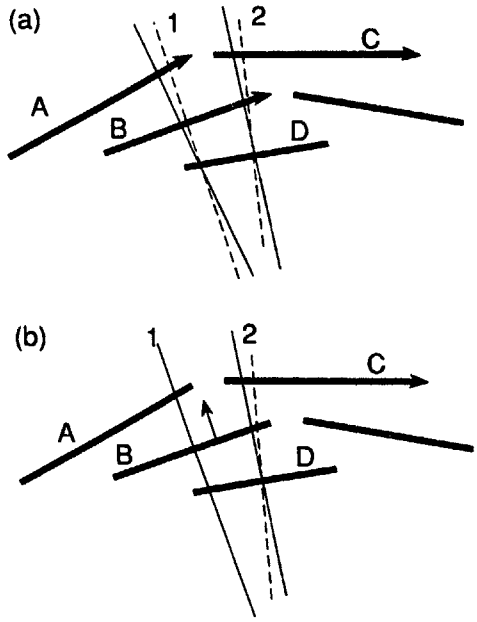

Fig. 37. Illustration of the constraints applied in the determination of the relative alignment of the SSVD modules from two tracks (thin solid lines) (a) for transverse displacement and (b) for both transverse and radial displacements of the detector modules (thick solid lines). The broken lines indicate the changes in the track direction for the displacements of the modules indicated by the arrows.

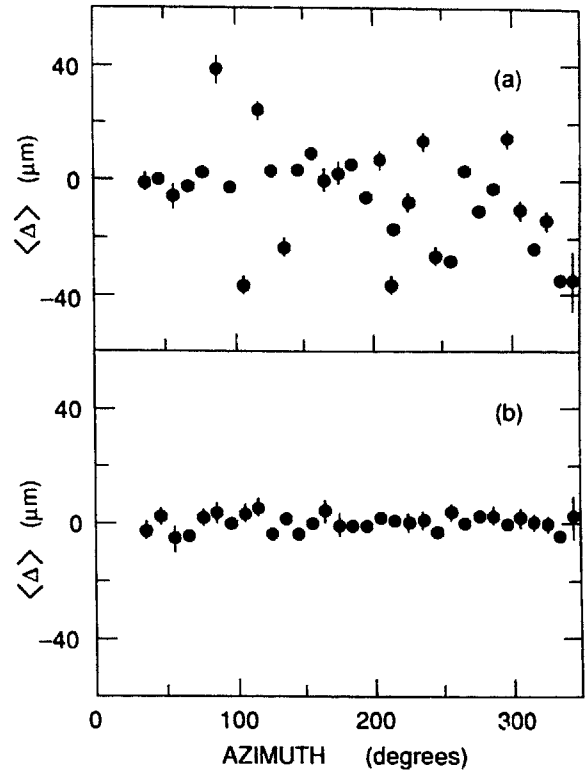

Fig. 38. Mean of the variable Δ as a function of azimuthal angle (a) before and (b) after the improvement of the local alignment constants. Each point corresponds to a different set of three overlapping detector modules. The first three points are missing because of the broken module in layer III.

9.4. *Intrinsic resolution*

With satisfactory internal alignment, the intrinsic position resolution of the silicon detectors can be derived from the measurement of the residuals of tracks with hits in all three layers of the SSVD. For this measurement, the tracks are defined by the measured positions in layer I and III, and the variable Δ is calculated as the signed distance of the measured point in layer II from the track, taking into account the track curvature and z position. Δ differs only slightly from the variable $\Delta\delta$ used in the alignment fits.

The improvement in the internal alignment of the SSVD is illustrated in fig. 38 which shows the mean value of Δ as a function of azimuthal position before and after the change in the constants. For most of the modules, the average Δ is centered about zero, as expected from the alignment fits. The widths of the Δ distributions can be used to measure the intrinsic position resolutions of silicon detectors. Fig. 39 shows the distribution of Δ for tracks with momenta greater than 1 GeV/c. A fit to a Gaussian distribution results in a standard deviation of 8.7 μm, corresponding to an average position resolution per layer of $\sigma = 8.7/\sqrt{3/2} = 7.1$ μm. This measurement is averaged over the three layers with strip pitches ranging from 25 to 33 μm, and tracks of non-normal incidence. It also includes measurement errors due to background hits overlapping with charged tracks. A Monte Carlo simulation reproduces the data very well. It is based on average point resolutions of 5, 6 and 7 μm in layers I, II, and III, respectively. Beam-related backgrounds effectively add 3 μm in quadrature to the resolution,

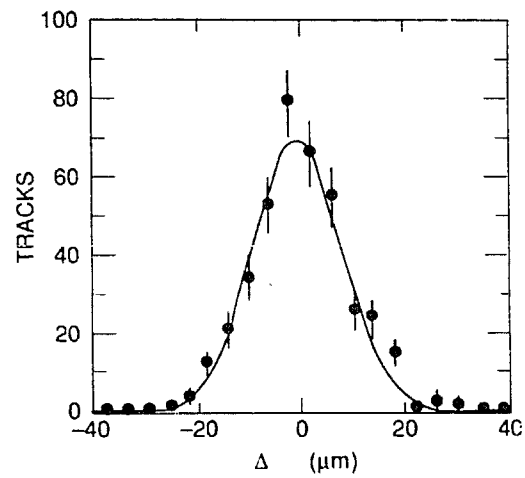

Fig. 39. Distribution of the variable Δ for tracks with momenta greater than 1 GeV/c. The data are compared to a Monte Carlo simulation (smooth curve).

while the uncertainties in the alignment constants add 2.5 μm.

9.5. *Impact parameter measurement*

The impact parameter is widely used to differentiate tracks that originate from different vertices in an event. It is particularly useful for relativistic particles because its average magnitude is proportional to the lifetime of the decaying particle and is nearly independent of its momentum. For this analysis, the impact parameter of a charged particle track was defined in the x–y plane as the signed distance of closest approach to the interaction point (IP) of the beam particles. The impact parameter is positive if the intersection of the track with the reconstructed trajectory of the decaying particle corresponds to a positive decay length; it is negative otherwise. The IP is a priori not known, but can be estimated either event by event or as the average vertex for several events recorded sequentially [39].

9.5.1. *Reconstruction of the interaction point*

In computing the average IP in the x–y plane, information from the SLC beam steering magnets was used to detect and correct for beam motion. For this purpose, the events were divided into six groups for which the IP position appeared relatively stable. For each group, the track positions were corrected event by event for beam motion predicted by the steering magnets, and a fit was done to determine a common vertex for all tracks. Although some of the tracks originated from secondary vertices due to particle decays or interactions, they had little effect on the average IP position because of the large number of tracks used in the fit. The SLC beam envelope had a typical rms width of less than 5 μm in both x and y, but the beam moved by much larger distances over the course of several hours. With rates of several hundred Z^0 per hour, the average vertex position could have given a very good estimate of the IP, only limited by the ability to monitor the beam position with time. However, during this run, time intervals between individual events were long and changes in the accelerator operating parameters were made continuously. Consequently, for this data sample, the uncertainty in the IP position was relatively large; it was dominated by beam motion and estimated to be of the order of 25 μm in both x and y.

To obtain an event-by-event estimate of the IP, the four tracks with the smallest distances of closest approach (DCA) to the average IP position in the x–y plane were selected. Of these four tracks, the subset of three tracks with the smallest DCAs and a vertex fit with a χ^2 probability greater than 1% was taken as the initial estimate for the IP position. Other tracks were added to this vertex, as long as the χ^2 probability of the vertex fit remained larger than 1%. This procedure was chosen so that tracks that did not originate from the beam–beam interaction point but from secondary interactions or decays did not strongly influence the determination of the primary vertex. The error in the vertex position was derived from the covariance matrices of the individual tracks. The resulting error ellipse for the event was usually aligned with the jet axis. The longitudinal error varied typically from 30 to 60 μm, while the error transverse to this axis varied from 5 to 15 μm. Due to the effects of poorly reconstructed tracks and secondary decay vertices, the actual uncertainties in the vertex position, as determined from a Monte Carlo simulation, were about a factor of two larger.

For the available data sample, a comparison between the average vertex position and the single event vertices showed that both methods of vertex finding lead to comparable uncertainties. The distribution of the differences between the average IP position and the single event vertex for events with at least seven selected tracks has an rms width of 29 μm, measured in the direction transverse to the jet axis. This width is much larger than the beam size (typically 5 μm), and also larger than the measurement error (roughly 18 μm) for the event by event vertex. It can be explained by an additional contribution to the uncertainty in the average vertex, attributed to motion of the beam with a rms width of 25 μm in both x and y. This is consistent with other measurements of the variation of the beam position, even after corrections based on steering magnet changes are made.

9.5.2. *Impact parameter resolution*

As a rough approximation, the impact parameter resolution is often written as a sum of two terms that are to be added in quadrature: a term that is largely momentum independent, and a second term due to multiple Coulomb scattering. The size of both terms depends on which of the three layers in the SSVD contribute to the measurement. The multiple scattering term was estimated to be of the order of 40–45 μm for tracks of 1 GeV/c momentum and two or more measurements in the SSVD. The first term can be thought of as a sum of several contributions. Their relative size has been estimated on the basis of the data and Monte Carlo simulations:

1) A geometric error that is dependent only on the intrinsic position resolution and geometry of the detector. Based on the measured position resolution in the silicon detector, this term is expected to be of the order of 7 μm for isolated tracks.

2) A term due to the effect of background hits on the position resolution that is estimated to contribute as much as 10 μm.

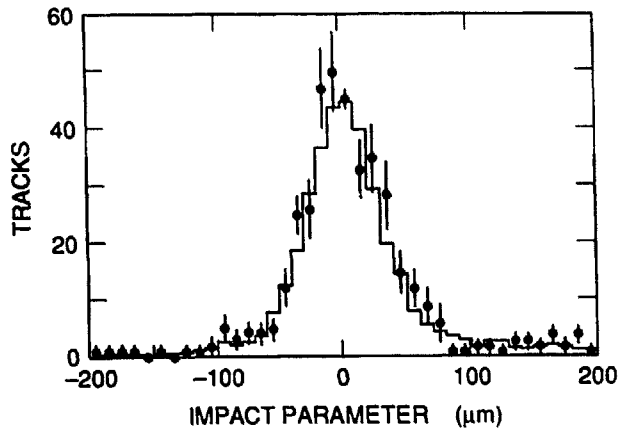

Fig. 40. The impact parameter measurement relative to the single-event vertex, for tracks with transverse momenta above 3.5 GeV/c. The points represent the measured tracks, the histogram shows the results of a detailed Monte Carlo simulation.

3) An error of about 15 μm due to the uncertainty in the relative placement of the individual detectors, which is dominated by the limited statistics of the data set.

4) An uncertainty of 20–25 μm in the position of the IP.

The error contributions listed above should be taken as estimates to illustrate the average relative size of the different effects. Not included in the list, nor in the standard Monte Carlo simulations, are uncertainties in the position and angular measurements in the outer tracking chambers, including the errors in their relative alignment and stability.

In fig. 40 the distribution of impact parameters measured relative to the event-by-event vertex is presented for tracks with momenta of more than 3.5 GeV/c. For the measurement of a given track in this plot, the track was removed from the determination of the vertex position and error. This procedure eliminated any bias in the impact parameter measurement, at the cost of an increased error. Under the assumption that all tracks in these hadronic events originated from a common vertex, this distribution measures the experimental resolution in the impact parameter. The measured distribution has a large peak in the center and sizable tails, both for positive and negative values. There is a small excess of particles in the positive tail, and this is attributed to the presence of tracks originating from secondary vertices. These tracks will not be discussed here, though they are of great interest to physics analyses [40]. A fit of the central peak to a Gaussian resolution function reproduces the data well and results in an rms width of 31 μm. Not included in fig. 40 is a small sample of Z^0 decays to pairs of charged leptons that can be used to measure the impact parameter resolution independent of the IP position. In these events, the distribution of the transverse miss distance of the two high momentum tracks near the IP has an rms width that translates to a measure of the impact parameter resolution, namely $\sigma_b = (35 \pm 7)$ μm$/\sqrt{2} = (25 \pm 5)$ μm. This measurement not only eliminates the uncertainty in the interaction point, but it is also free of tracking errors caused by signals from nearby charged tracks in the event.

Comparisons between the data and Monte Carlo simulations were performed over the complete momentum spectrum. By taking into account the detector geometry, resolution, and efficiency as well as effects of multiple scattering, beam background and alignment errors fairly good agreement was achieved, though the width of the Gaussian core and the tails of the impact parameter distribution were somewhat smaller than for the data. To improve the comparison for low momentum tracks, the multiple scattering was enhanced by increasing the material in the vacuum pipe and the detectors by 10% in the simulation. This change was not unreasonable, given the uncertainty in the treatment of the scattering and the composition of the detector elements. To account for remaining differences between the data and the Monte Carlo, primarily the size of the tail at negative values of the impact parameter, a Gaussian error with a width of 75 μm was added to 15% of the simulated tracks, selected at random. The source of this additional error is not fully understood. It probably accounts for underestimates of uncertainties in the tracking and vertexing due to systematic effects that are not included in the simulation. For instance, there are clear indications that, independent of the SSVD, the track errors in the drift chambers were larger and less uniform than assumed. The improved Monte Carlo distribution is shown in fig. 40 and agrees well with the data, both for the peak and the tails.

The variance of the impact parameter distributions, obtained from fits of the core of the distributions to Gaussian resolution functions, are shown in fig. 41a as a function of K^2, where $K = 1/(p_{xy}\sqrt{\cos\lambda})$. The data, averaged over all tracks, are shown together with the results of detailed Monte Carlo simulations, including the increased tracking errors for a random subsample of the tracks. With these adjustments of the Monte Carlo, good agreement is achieved over the entire momentum range. For comparison, fig. 41b shows the calculated resolution for different combinations of hits in the SSVD. The calculation assumes perfect track reconstruction and no uncertainty in the position of the IP. As expected, tracks with hits in the first and third SSVD layer (or all three layers) have the best resolution. Tracks with only one associated hit in the SSVD are more sensitive to the resolution in the VDC, and thus their resolution varies due to the cell structure of the VDC. At the highest momenta, the position

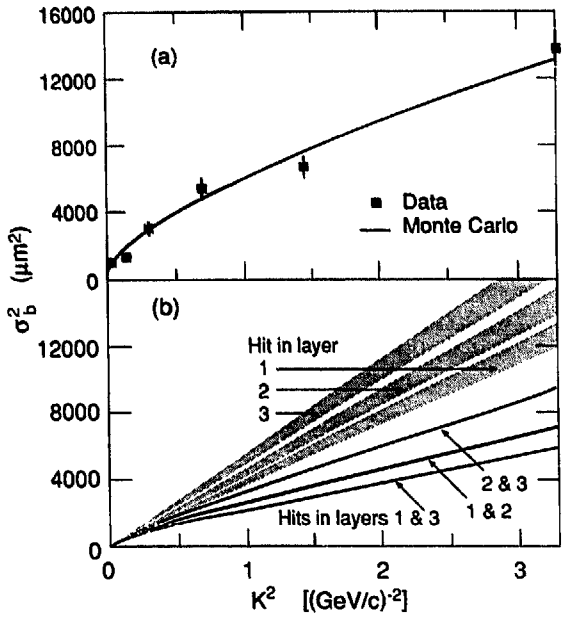

Fig. 41. Measured and calculated resolution in the transverse impact parameter as a function of K^2, where $K = 1/(p_{xy}\sqrt{\cos\lambda})$: (a) the measured resolution for the data sample and Monte Carlo simulated tracks, as described in the text; (b) the calculated resolution assuming perfect track reconstruction and no uncertainty in the IP position. The different lines correspond to different combinations of SSVD hits associated with tracks. For single hit tracks, the grey regions represent the variations due to changes in the VDC resolution across the cells.

resolution of the silicon strip detector is most important and it is combined with the excellent measurement of the track angle ϕ in the wire chambers. As the track momentum decreases, increased multiple scattering in the SSVD and the drift chamber walls degrades the angle measurement in the wire chambers. Thus for lower momenta, the angular information from the SSVD becomes more important and multiple SSVD hits per track improve the resolution compared to tracks with a single SSVD hit.

The difference between the best calculated resolution (which is also shown in fig. 1) and the data in the top half of fig. 41 illustrates the combined effect of all the sources of additional errors that contribute to the measurement of the track impact parameters in hadronic Z^0 decays.

10. Summary and conclusions

A silicon strip detector composed of 36 detector modules with VLSI readout has been successfully designed, built, and operated as a precision vertex detector in the Mark II experiment at the SLC. While the assembly represented a major challenge at all stages, the completed device performed well and largely as designed:

1) Of the 18396 electronics readout channels only a small fraction, less than 1.6%, failed because of detector defects or malfunctioning amplifier or readout circuits. The most severe loss was caused by two cables that were broken, one during installation into the SSVD, the other while the Mark II endcaps were being closed.

2) The system was very reliable and stable during the eleven months of operation at the Stanford Linear Collider. There were occasional large shifts in the pedestals of individual detector modules, and there was some evidence that these shifts were correlated with instantaneous beam losses.

3) The detectors were highly efficient for the detection of charged particles. The observed signal-to-noise ratio was approximately 18:1.

4) The position resolution, averaged over tracks in three layers with strip pitches between 25 and 33 μm and including tracks of non-normal incidence, was measured to be 7.1 μm. This measurement also included the effect of background hits overlapping with tracks.

5) A substantial effort went into the survey of the relative placement of the individual detector modules prior to installation on the beam pipe. Though both techniques succeeded in determining the placement and shape of the detectors at the time of measurement to the level of a few μm in position, and better than 0.03 mrad in angle, it was necessary to repeat and update the survey using charged particle tracks from the beam. The error in the relative placement of the detector modules was limited by the number of tracks available, and by the uncertainties in the position and angular measurements in the outer tracking chambers, including errors in their relative position and stability.

6) A system of capacitive displacement monitors was installed to track motion of the SSVD relative to the vertex drift chamber. It performed well and proved very useful in signaling major disturbances in the SSVD position.

7) The resolution in the impact parameter was not primarily determined by the intrinsic resolution in the SSVD, but it was strongly influenced by the uncertainty in the vertex position, multiple scattering in the beam pipe and the detectors, the uncertainty in the alignment and the errors in the track measurement in the surrounding tracking chambers. The resolution was dependent on the number of measurements in the SSVD, and the density of tracks and background hits. The resolution can be fairly well reproduced by a detailed Monte Carlo simulation of the track and vertex reconstruction. Differences can be accounted for by

the addition of an error distribution with an rms width of 75 μm to 15% of the tracks.

The SSVD performed well at the SLC. Its efficiency and intrinsic resolution are well understood. The overall impact parameter resolution could have been substantially better, had it not been for the limited statistics, the relatively large fluctuations in the beam position, and the substantial beam related background in the detector during this first operation at the SLC, a machine of novel design. Nevertheless, based on this vertex detector system, a technique has been developed and sucessfully applied to select a clean sample of hadronic $b\bar{b}$ events with high efficiency and to measure the coupling of the Z^0 to beauty quarks [40].

With much larger statistics, the errors in the alignment and the position of the IP could possibly be reduced to the level where the monitoring accuracy becomes the limiting factor. In future designs, the dependence of the alignment accuracy and the impact parameter measurement on the position and angle measurement in the outer tracking chambers could be minimized in a silicon vertex detector with much larger spacing of the layers. Similarly, a detector with small overlaps rather than gaps between modules in a given layer is expected to achieve a better and more uniform resolution for tracks at all angles.

Acknowledgements

The design, construction and installation of the SSVD represented a substantial effort over several years and would not have been possible without the advice, support, and active participation of a large number of persons. We cannot thank everyone of them, but we particularly commend M. Lateur, W. Nilsson, and M. Studzinski for their contribution to the mechanical design and construction of many parts, and D. Hutchinson and J. Tinsman for their assistance with the design of the data acquisition system. We are also indebted to the Stanford Synchrotron Radiation Laboratory for the support and kind hospitality during the alignment measurements. We should like to express our appreciation to members of the SLAC staff and many of our colleagues from collaborating universities for their dedicated effort of operating this innovative e^+e^- collider. Finally, we thank our colleagues of the Mark II collaboration for the operation of the Mark II detector, and the members of the VDC group, in particular D. Fujino, J.A. Jaros, D.S. Koetke, B.A. Schumm, and S.R. Wagner, for their competitive spirit and their numerous contributions to the wire chamber tracking, as well as to the impact parameter measurement.

References

[1] R. Bailey et al., Nucl. Instr. and Meth. 226 (1984) 56.
[2] J.T. Walker et al., Nucl. Instr. and Meth. 226 (1984) 200.
[3] G. Anzivino et al., Nucl. Instr. and Meth. A243 (1986) 153.
[4] G. Abrams et al., Nucl. Instr. and Meth. A281 (1989) 55.
[5] G. Hanson et al., Nucl. Instr. and Meth. A252 (1986) 343.
[6] J.P. Alexander et al., Nucl. Instr. and Meth. A283 (1989) 519.
[7] D. Durrett et al., Calibration and Performance of the Mark II Drift Chamber Vertex Detector, in: Proc. 5th Int. Conf. on Instrumentation for Colliding Beam Physics, Novosibirsk, USSR (1990).
[8] C. Adolphsen et al., Nucl. Instr. and Meth. A253 (1987) 444.
[9] Hamamatsu Photonics KK, Hamamatsu City, Japan; S2910 Series of MicroStrip Detectors.
[10] J. Kemmer, Nucl. Instr. and Meth. 169 (1980) 499.
[11] Micron Semiconductor Ltd., Lancing, Sussex, UK.
[12] M. Nakamura et al., Nucl. Instr. and Meth. A270 (1988) 42.
[13] Gould-AMI, Santa Clara, CA, USA, and Pocatello, ID, USA.
[14] P. Dauncey et al., IEEE Trans. Nucl. Sci. NS-35 (1988) 166;
A. Breakstone et al., IEEE Trans. Nucl. Sci. NS-34 (1987) 491.
[15] S.I. Parker, Nucl. Instr. and Meth. A275 (1989) 499.
[16] Kapton is a polyimide film with a volume resistivity of 10^{12} Ω/cm, and a dielectric constant 4.0, registered trademark by DuPont, Wilmington, DE, USA.
[17] HEXFET IRFC030 or equivalent.
[18] Promex, Santa Clara, CA, USA.
[19] PCB, Santa Clara, CA, USA, and General Circuits, Menlo Park, CA, USA.
[20] Prima-Bond EG7650, produced by A.I. Tech Incorporated, Princeton, NJ, USA.
[21] TRA-BOND BA 2115, produced by Tracon, Medford, MA, USA.
[22] Silver-filled room temperature curing epoxy, product 50-02-0584-0029 by Chromerics, Woburn, MA, USA.
[23] EPO-TEK 509F, produced by Epoxy Technology, Billerca, MA, USA.
[24] Product #14250, Devcon Corporation, Danvers, MA, USA.
[25] M. Breidenbach et al., IEEE Trans. Nucl. Sci. NS-25 (1978) 706.
[26] G. Lutz, Max-Planck-Institut, München, preprint MPI-PAE 173 (1987).
[27] C. Adolphsen et al., IEEE Trans. Nucl. Sci. NS-35 (1988) 424.
[28] HFBR-1404, produced by Hewlett & Packard, Palo Alto, CA, USA.
[29] Bausch & Lomb Stereozoom-7, object magnification 7.
[30] C. Adolphsen et al., Nucl. Instr. and Meth. A288 (1990) 257.
[31] Assembled by Technical Instruments of San Francisco, CA, USA, with Nikon optics, magnification 10×40, and Heidenhain digital readout.
[32] Alessi Inc., Irvine, CA, USA, Probe station accessories PTT-06 and PTT-12.

[33] A. Breakstone et al., Nucl. Instr. and Meth. A281 (1989) 453;
A. Breakstone, Nucl. Instr. and Meth. A305 (1991) 39.
[34] HPB-150 sensors with dual channel amplifiers model 3200-S-WB by Capacitec Inc., Ayer, MA 01432, USA.
[35] J. Perl et al., Nucl. Instr. and Meth. A252 (1986) 616.
[36] Multiple scattering was modeled using the full Molière distribution to account for non-Gaussian tails. Subroutine MLR, CERN Program Library.
[37] C. Adolphsen, Mark II/SLC Note 266 (1990) unpublished.
[38] R.G. Jacobsen, PhD Thesis, Stanford University, SLAC-381 (1991).
[39] S.R. Wagner, private communication.
[40] R.G. Jacobsen et al., Measurement of the $b\bar{b}$ Fraction in Hadronic Z^0 Decays with Precision Vertex Detectors, submitted to Phys. Rev. Lett. (1991), SLAC PUB-5603.